DEVELOPMENT OF A BURST MODE OSCILLATOR FREE FEMTOSECOND FIBER LASER

A THESIS SUBMITTED TO
THE GRADUATE SCHOOL OF NATURAL AND APPLIED SCIENCES
OF
MIDDLE EAST TECHNICAL UNIVERSITY

BY

HÜR DOĞA KANTOĞLU

IN PARTIAL FULFILLMENT OF THE REQUIREMENTS
FOR
THE DEGREE OF MASTER OF SCIENCE
IN
PHYSICS

JANUARY 2023

Approval of the thesis:

DEVELOPMENT OF A BURST MODE OSCILLATOR FREE FEMTOSECOND FIBER LASER

submitted by **HÜR DOĞA KANTOĞLU** in partial fulfillment of the requirements for the degree of **Master of Science** i**n Physics, Middle East Technical University** by,

Prof. Dr. Halil Kalıpçılar
Dean, Graduate School of **Natural and Applied Sciences** _____

Prof. Dr. Seçkin Kürkcüoğlu
Head of the Department, **Physics** _____

Assist. Prof. Dr. Ihor Pavlov
Supervisor, Physics**, METU** _____

Examining Committee Members:

Assist. Prof. Dr. Parviz Elahi
Physics**,** Boğaziçi University _____

Assist. Prof. Dr. Ihor Pavlov
Physics, METU _____

Assoc. Prof. Dr. Emre Yüce
Physics, METU _____

Date: 25.01.2023

I hereby declare that all information in this document has been obtained and presented in accordance with academic rules and ethical conduct. I also declare that, as required by these rules and conduct, I have fully cited and referenced all material and results that are not original to this work.

Name Last name: Hür Doğa Kantoğlu

Signature:

ABSTRACT

DEVELOPMENT OF A BURST MODE OSCILLATOR FREE FEMTOSECOND FIBER LASER

Kantoğlu, Hür Doğa
Master of Science, Physics
Supervisor: Assist. Prof. Dr. Ihor Pavlov

January 2023, 60 pages

Lasers with short pulse duration have a wide range of applications in industry and science, such as telecommunication, processing, imaging, and metrology. A conventional and well-known method for producing short pulses is mode locking. However, mode locking ultrashort lasers have a limitation on repetition rate because of the cavity length. Several techniques have been proposed to overcome this limitation, such as harmonic mode locking and adding a repetition rate multiplier into a system. Nevertheless, these methods increase system complexity and cost.

High repetition rate ultrashort lasers are highly desired due to their promising capabilities in material processing as well as nonlinear optics and optical sampling. Usually adding a modulator into a high repetition rate source makes the laser operate on a burst mode regime with unique applications such as ablation cooled processing regime.

In this study, a pulsed laser is created by combining two continuous-wave lasers and then the beat pulse is broadened by four-wave mixing. After the broadening, the beat pulse is compressed by the negative dispersion fiber. Our oscillator free laser system

produces femtosecond pulses with picosecond pulse energy and tunable GHz intra-burst repetition rate which is suitable for material processing.

Keywords: Femtosecond Laser, Burst Mode Laser, Four-Wave Mixing

ÖZ

KÜME MODLU OSİLATÖRSÜZ FEMTOSANİYE FİBER LAZER GELİŞTİRİLMESİ

Kantoğlu, Hür Doğa
Master of Science, Physics
Supervisor : Assist. Prof. Dr. Ihor Pavlov

Ocak 2023, 60 sayfa

Kısa atım süresine sahip lazerler, telekomünikasyon, malzeme işleme, görüntüleme, metroloji gibi endüstride ve akademide geniş bir uygulama yelpazesine sahiptir. Mod kilitleme, kısa atım oluşturmak için iyi bilinen ve geleneksel bir yöntemdir. Fakat mod kilitlemeli ultra-kısa lazerlerin tekrar frekansı kavite uzunluğundan dolayı sınırlıdır. Bu sınırlamanın üstesinden gelmek için, harmonik mod kilitleme ve sisteme tekrar frekansı çoğaltıcı ekleme gibi çeşitli teknikler önerilmiştir. Bununla birlikte, bu yöntemler sistemin karmaşıklığını ve maliyetini artırır.

Yüksek tekrar frekanslı ultra-kısa lazerler, lineer olmayan optic ve optik örnekleme dışında malzeme işleme gibi gelecek vadeden uygulamalarından dolayı epey arzu edilir. Genellikle, yüksek tekrar frekanslı bir sisteme modülatör ekleyerek lazeri ablasyon soğumalı malzeme işleme gibi niş uygulamalara sahip küme modlu lazer modunda çalışmasını sağlar.

Bu çalışmada, atım lazeri iki sürekli lazeri birleştirerek oluşturulmuştur ve ardından bu atımın spektrumu dört dalga karışımıyla genişletilmiştir. Genişlemenin ardından, bu atım negatif dispersiyon fiber tarafından sıkıştırılmıştır. Osilatörsüz lazer

sistemimiz, malzeme işlemeye uygun, pikojül atım enerjisi ve ayarlanabilir GHz tekrarlama frekansı ile femtosaniye atımlar üretir.

Anahtar Kelimeler: Femtosaniye Lazer, Küme Modlu Lazer, Dört Dalga Karışımı

To all my family and friends…

ACKNOWLEDGMENTS

I would like to express my deepest gratitude to my supervisor Assist. Prof. Dr. Ihor Pavlov for his guidance throughout the research. He was always there with his continuous support and patience when I needed it.

I would like to express my sincere gratitude to Dr. Arian Goodarzi for his suggestions and comments through the research.

I would like thank my family for their unlimited encouragement and love in my whole life.

TABLE OF CONTENTS

LIST OF TABLES

TABLES

LIST OF FIGURES

LIST OF ABBREVIATIONS

HNLF	Highly Nonlinear Fiber
SMF	Single Mode Fiber
NA	Numerical Aperture
GVD	Group Velocity Dispersion
FWM	Four-Wave Mixing
SPM	Self-Phase Modulation
DCF	Dispersion Compensating Fiber
EDFA	Erbium-Doped Fiber Amplifier
YDFA	Ytterbium-Doped Fiber Amplifier
AOM	Acousto-Optic Modulator
WDM	Wavelength Division Multiplexer
MPC	Multimode Pump Combiner
HWP	Half Wave Plate
PBS	Polarizing Beam Splitter
FROG	Frequency Resolved Optical Gating

CHAPTER 1

INTRODUCTION

Stimulated emission is the fundamental mechanism for lasers which was first proposed by Einstein in 1917 [1]. After decades, the first laser was invented by Theodore H. Maiman in 1960 [2]. Lasers are classified by their gain medium. The first laser is a solid-state laser that made use of ruby crystal as the gain medium. Each gain medium results in different gain-linewidth, hence various properties such as the pulse duration as can be seen from the following figure [3].

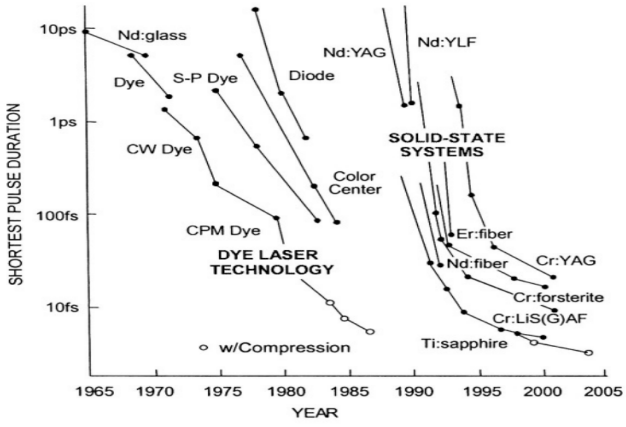

Figure 1.1 The evolution of ultrashort pulse duration

The invention of ultrashort optical pulses with a duration of few picoseconds to femtoseconds took its place in various applications such as optical metrology, laser processing, imaging and ultrafast optical communications [4,8]. The most basic technique for producing ultrashort pulses is placing a modulator into a system or gain

switching method to modulate the laser diode. However, these methods have major drawbacks due to dependence on external optical or electrical devices, hence pulse duration is limited by the response time and bandwidth of the device.

Mode locking is one of the most common techniques for producing ultrashort pulses. Nevertheless, the repetition rate of the pulses which are created by the mode locking method depends on cavity length. One method for reaching higher repetition rates is harmonic mode locking, however this method makes the system more complex [9]. Repetition rate multiplier is another solution, yet the maximum repetition rate is limited by the minimum achievable fiber length difference [10]. High repetition rate ultrashort pulse sources play a vital role in the areas of fiber optic communications, material processing and spectroscopy [11,13]. Adding a modulator into a high repetition laser system forms a burst mode laser which has a unique application such as ablation cooled material removal [14].

A promising way to achieve a high repetition rate ultrashort pulse is combining two continuous waves with slightly different frequencies to form a beat and then send it through the nonlinear medium. Hence, the initial beat signal is compressed by the multiple four-wave mixing while the spectrum broadens until phase mismatch occurs. The first analytical expression of a beat signal experiencing four-wave mixing inside the fiber was conducted in 1994 by Trillo [15]. After that, ranging from a few gigahertz to terahertz repetition rate ultrashort pulses are obtained through the highly nonlinear fiber (HNLF), single mode fiber (SMF) and photonic crystal fiber [16,21]. In this thesis, a burst mode femtosecond laser is created by the propagation of a beat signal inside the dispersion compensating fiber with a higher nonlinear coefficient compare to SMF due to small core diameter

CHAPTER 2

THEORETICAL BACKGROUND OF FIBER LASER AND LASER-MATTER INTERACTIONS

In this section, the fundamentals of fiber laser and nonlinear interactions will be discussed.

2.1 Fiber Optics

The most basic fiber design is a single clad step index fiber as shown in Figure 2.1. The single clad step index fiber has a core, cladding and coating with refractive indexes n_1, n_2, n_3 respectively. The refractive indexes are adjusted by adding a particular amount of dopant in such a way that the refractive index of the core is higher than the refractive of the cladding so that total internal reflection occurs between the core and the cladding.

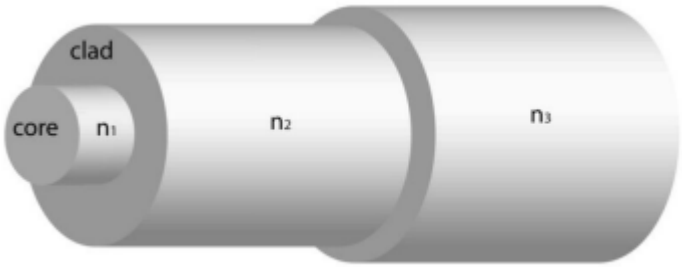

Figure 2.1 A Step index fiber

The light which coupled from the medium with refractive index n_0 into a core of the fiber does not propagate if the angle is lower than the critical angle. The critical angle is the minimum angle for total internal reflection to happen as given by Equation 2.2. Therefore, total internal reflection imposes a constraint on the entrance angle α as illustrated in Figure 2.2.

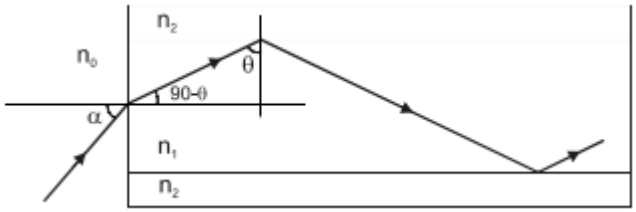

Figure 2.2 Light coupling into a fiber

Where, n_1 and n_2 are the refractive indexes of the core and the cladding of the fiber. By applying Snell's law to the boundary between n_0 and n_1 , the maximum entrance angle α_{max} can be written as

$$n_0 \sin \alpha_{max} = n_1 \sin(90^o - \theta_c) \quad (2.1)$$

$$sin\theta_c = \frac{n_2}{n_1} \quad (2.2)$$

Equations 2.1, 2.2 and the trigonometric identities $\sin(90^0 - \theta_c) = cos\theta_c = \sqrt{1 - sin\theta_c^2}$ can be all combined as

$$n_0 \sin \alpha_{max} = \sqrt{n_1^2 - n_2^2} \quad (2.3)$$

The square root term of Equation 2.3 is defined as a numerical aperture (NA). The NA is a dimensionless quantity which shows the maximum entrance angle that supports total internal reflection [22]. The NA is expressed as,

$$NA = n_1(2\Delta)^{\frac{1}{2}} = n_1 \left[2\left(\frac{n_1-n_2}{n_1}\right)\right]^{1/2} \quad (2.4)$$

Where, Δ is the fractional refractive index. Another dimensionless parameter V which determines the number of propagating modes inside the core can be given as

$$V = \frac{2\pi}{\lambda}\, a\ NA \quad (2.5)$$

Where, a is the radius of the core and $\frac{2\pi}{\lambda}$ is the wave vector of the light. If the parameter V is smaller than 2.405, then only a single mode propagates inside the core. If it is higher than 2.405, then by analyzing the mode chart the number of modes is determined [22].

2.2 Dispersion

Generally, dispersion is responsible for broadening the pulse in time inside the core of the fiber. Each mode has different speeds for multimode propagation, which cause broadening and is called intermodal dispersion. In the case of single mode propagation, there is no intermodal dispersion. However, due to the source's finite spectral width, each wavelength component has different speeds causing broadening in time, and it is called intramodal dispersion or chromatic dispersion.

2.2.1 Group Velocity Dispersion

The origin of group velocity dispersion (GVD) is related to the wavelength dependence of the refractive index of the material. The group velocity of the pulse can be defined as Equation 2.6. Where, β represents the axial wave vector component and equal to $n_{eff}\frac{2\pi}{\lambda}$. The n_{eff} is the effective refractive index experienced by the mode of the fiber. Its value is between n_1 and n_2 [22].

$$v_g = \left(\frac{d\beta}{d\omega}\right)^{-1} \quad (2.6)$$

The group velocity can also be calculated from the group refractive index , n_g , as shown in Equations 2.7 and 2.8.

$$v_g = \frac{c}{n_g} \tag{2.7}$$

$$n_g = n_{eff} + \omega \frac{dn_{eff}}{d\omega} \tag{2.8}$$

The time for the pulse to propagate inside the fiber varies for each frequency component. The time delay depends on the spectral width of the pulse, length and β_2 parameter which is called the GVD parameter as given by Equation 2.9.

$$\delta t = \frac{dt}{d\omega}\delta\omega = \frac{d}{d\omega}\left(\frac{L}{v_g}\right)\delta\omega = L\,\beta_2\,\delta\omega \tag{2.9}$$

The time delay can also be constructed by taking the derivative respect to the wavelength as shown by Equation 2.10. Where, D is the dispersion parameter and it is related by the GVD parameter as can be seen by Equation 2.11.

$$\delta t = \frac{dt}{d\lambda}\delta\lambda = \frac{d}{d\lambda}\left(\frac{L}{v_g}\right)\delta\lambda = D\,L\,\delta\lambda \tag{2.10}$$

$$D = \frac{d}{d\lambda}\left(\frac{1}{v_g}\right) = -\frac{2\pi c}{\lambda^2}\,\beta_2 \tag{2.11}$$

Consider a new parameter which is known as normalized propagation constant b as introduced by

$$b = \frac{n_{eff} - n_2}{n_1 - n_2} \tag{2.12}$$

When the refractive indexes are almost equal, effective refractive n_{eff} is approximated as shown by Equation 2.13 [22].

$$n_{eff} \approx n_2\,(1 + b\Delta) \tag{2.13}$$

Dispersion parameter can be also written in terms of frequency derivative as given by

$$D = -\frac{2\pi}{\lambda^2}\frac{d}{d\omega}\left(\frac{1}{v_g}\right) = -\frac{2\pi}{\lambda^2}\left(2\frac{dn_{eff}}{d\omega} + \omega\frac{d^2n_{eff}}{d\omega^2}\right) \quad (2.14)$$

Replacing n_{eff} according to Equation 2.13, then using Equation 2.5 decomposes the dispersion parameter by two components such as material dispersion , D_m , and waveguide dispersion , D_W, as shown by following Equations 2.15, 2.16 and 2.17 [22].

$$D = D_m + D_W \quad (2.15)$$

$$D_m = \frac{1}{c}\frac{dn_{2g}}{d\lambda} \quad (2.16)$$

$$D_w = -\frac{2\pi\Delta}{\lambda^2}\left[\frac{n_{2g}^2}{n_2\omega}\frac{Vd^2(Vb)}{dV^2} + \frac{dn_{2g}}{d\omega}\frac{d(Vb)}{dV}\right] \quad (2.17)$$

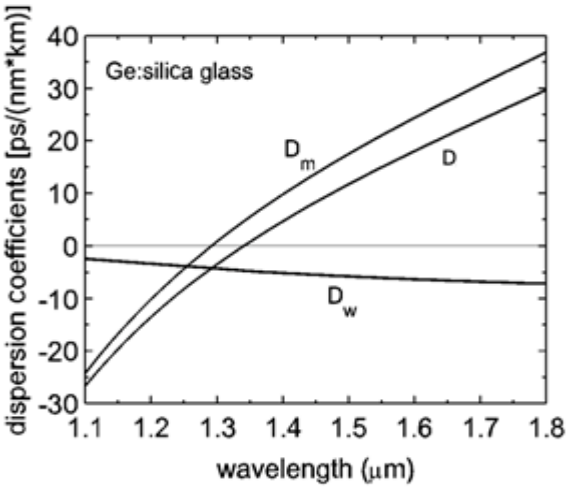

Figure 2.3 The dispersion coefficients of the silica glass

According to Figure 2.3, material dispersion becomes positive for wavelengths higher than 1.276 μm, which means shorter wavelengths travel faster. A positive dispersion parameter regime is called anomalous dispersion. Material dispersion becomes negative for wavelengths lower than 1.276 μm thus, shorter wavelengths

travel slower. A negative dispersion parameter regime is called normal dispersion. 1.276 μm is zero dispersion wavelength, and waveguide dispersion shifts this wavelength to 1.31 μm. Waveguide dispersion can be adjusted by tailoring the core radius and/or fractional refractive index. Hence, zero dispersion wavelength can be relocated to a telecommunication wavelength of 1.55. This fiber is called dispersion shifted fiber. Moreover, the dispersion can be flattened between telecommunication ranges, called dispersion flattened fiber [23]. Dispersion is not completely disappeared at zero dispersion wavelength. The contribution of higher order terms, such as third order dispersion becomes dominant at zero dispersion wavelength. Even at nonzero dispersion wavelength, if the initial pulse width is shorter than 1ps, the third order dispersion effects must be included [24].

When the pulse's instantaneous frequency increases (decreases), it is called a positive (negative) chirp. The dispersion becomes significant if the fiber length is comparable with the dispersion length $L_d = \frac{T_o^2}{|\beta_{2|}}$. Where, T_0 is the initial pulse width. Dispersion changes the shape of the pulse inside the fiber. However, for an input Gaussian pulse, whether it is initially chirped or not, the shape remains Gaussian. If the input pulse is Gaussian and unchirped, then pulses become negative (positive) chirped in an anomalous (normal) dispersion regime [24].

2.3 Nonlinear Effects

The interaction of light and matter becomes nonlinear if the material's response to light depends on the light's electric field nonlinearly. Nonlinear effects occur when the electric field of the wave thus intensity is large enough which is the case for the laser beam propagating through the fiber. Similar to the dispersion case, nonlinear effects become dominant when the fiber length, L, is comparable with the nonlinear length $L_{NL} = \frac{1}{\gamma P_o}$. Where P_o is the peak power of the pulse and γ is the nonlinear coefficient of the fiber [24].

Material response is characterized as polarization. Polarization is related to the electric field by the relation given by Equation 2.18. Note that, higher order terms of susceptibility are neglected and the equation is simplified in just one dimension although it is a tensor equation [24].

$$P_x = \epsilon_o(\chi_1 E_x + \chi_2 E_x^2 + \chi_3 E_x^3) \tag{2.18}$$

Where, ϵ_o is the permittivity of free space and χ_1, χ_2, χ_3 is linear (first), second and third order susceptibilities respectively. Certain materials which have inversion symmetry such as glass, χ_2 is equal to zero and these materials are called centrosymmetric. Noncentrosymmetric materials such as KDP and $LiNbO_3$ which have no inversion symmetry, the χ_2 is not zero [23]. Although silicon is centrosymmetric material it can exhibit second order susceptibility properties under applied electric field and stress [25,26].

2.3.1 Four-wave mixing

A straightforward approach for the light interacting with the centrosymmetric material is made by assuming the light is monochromatic, as shown in Equation 2.19.

$$E(t) = A\cos\omega t \tag{2.19}$$

By putting Equation 2.19 into 2.18 for the case of $\chi_2 = 0$ and using trigonometric identity $\cos^3\theta = (3cos\theta + cos3\theta)/4$ resulted in following Equations 2.20 and 2.21 [23].

$$P_\omega = \epsilon_o A(\chi_1 + (3/4)\,\chi_3 A^2) \tag{2.20}$$

$$P_{3\omega} = \frac{1}{4}\epsilon_o\,\chi_3 A^3 \tag{2.21}$$

The term P_ω and $P_{3\omega}$ is radiated light at frequencies same as incident light and three times the incident light which is known as a third harmonic generation. Third harmonic generation is a subclass of four wave mixing. Four-wave mixing (FWM) occurs when three optical waves with frequencies $\omega_1, \omega_2, \omega_3$ are combined and interact with the χ_3 medium, new wave with the frequency ω_4 is generated in combination of $\omega_4 = \omega_1 \pm \omega_2 \pm \omega_3$ incident optical waves. The most common process is the degenerate four-wave mixing which is the case for $\omega_1 = \omega_2$. The other combinations may also occur but satisfying phase matching condition is cumbersome. FWM can also be explained as two photons with frequencies ω_1, ω_2 are destroyed and the new photons with frequencies ω_3, ω_4 are created if the energy and the momentum conservations are satisfied. Furthermore, created photons ω_3, ω_4 interact with ω_1, ω_2 and new photons are generated ω_5, ω_6 as shown in Figure 2.4 [23]. This process will continue until phase mismatch occurs and it is called cascaded four-wave mixing or multiple FWM [27].

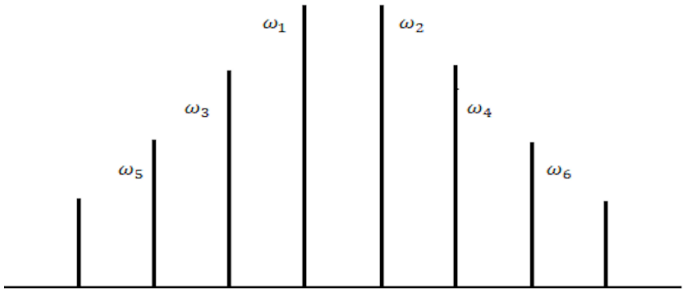

Figure 2.4 Schematic view of cascaded four-wave mixing

2.3.2 Nonlinear refractive index

χ' is the effective susceptibility deduced from the parenthesis term in Equation 2.20.

$$\chi' = (\chi_1 + (3/4)\,\chi_3 A^2) \tag{2.22}$$

Since the refractive index depends on the susceptibility, by using the equation $I = \frac{1}{2}\, c\, n\, \epsilon_o\, A^2$, the refractive index dependence of the intensity can be seen in Equation 2.23 [23].

$$n = n_0 + n_2'\, I \tag{2.23}$$

Where, n_2' is the nonlinear refractive index and it can be written as

$$n_2' = \frac{3\chi_3}{4\, n^2 c\, \epsilon_o} \tag{2.24}$$

Commercial single mode fiber's nonlinear refractive index value is approximately $2.6x10^{-20} m^2 / W$ and changes with a dopant such as GeO_2. Much higher nonlinear refractive indexes are reached by adding bismuth-oxide or lead-silicate [24].

The nonlinear coefficient ,γ, depends on nonlinear refractive index as given by Equation 2.25.

$$\gamma = \frac{2\pi}{\lambda} \frac{n_2'}{A_{eff}} \tag{2.25}$$

Where, A_{eff} is the effective mode area. HNLF is fabricated by adding a dopant with a high nonlinear refractive index and decreasing the core radius hence the effective mode area. The typical value of the nonlinear coefficient for conventional HNLF is around 20 $W^{-1}m^{-1}$ [28].

2.3.3 Self Phase Modulation

Since the refractive index depends on the intensity, the propagation constant ,k, also depends on intensity as follows

$$k = \frac{n\,\omega}{c} = \frac{n_0\,\omega}{c} + \frac{n_2' I\,\omega}{c} = k_0 + \Delta k \tag{2.26}$$

Intensity dependent propagation constant leads to intensity dependent phase shift which is called self-phase modulation as given by Equation 2.27.

$$\Delta\phi = \Delta k L = k_0 n_2' I L \tag{2.27}$$

Note that when the intensity is constant in time as in the case of continuous wave laser, the time derivative of phase by mean frequency does not change. In the case of a pulse propagating through the nonlinear medium frequency changes with time.

$$\omega = \frac{d\phi}{dt} = \omega_0 - n_2' k_0 L \frac{dI}{dt} \tag{2.28}$$

The frequency chirp depends on the phase of the pulse. For a gaussian pulse, the chirp is linear and positive only in the middle portion of the pulse in the time domain. As the pulse propagates through the fiber, new frequency values are created by the self-phase modulation (SPM). Therefore, the spectrum broadens unless the input pulse is negatively chirped [23,24]. Spectral broadening also depends on spectral width which is related to the pulse duration. Consequently, SPM induced spectral broadening would be very high for a short pulse and result in a supercontinuum [29].

2.3.4 Optical Soliton

The soliton forms when the pulses propagate in an anomalous dispersion regime. The SPM induced positive chirp compensated by negative chirp arose from anomalous dispersion [24].

$$N^2 = \frac{T_o^2 \gamma P_o}{|\beta_{2|}} \tag{2.29}$$

The parameter N is the ratio of dispersion length divided by the nonlinear length which determines the soliton order as shown in Equation 2.29. When the parameter N equals to one, the soliton is referred as the fundamental soliton. One of the most remarkable properties of the soliton is that it preserves its shape continuously in the case of fundamental soliton or in a periodic fashion in the case of higher order solitons while propagating through the fiber. The soliton is very stable and alters its width and shape when it is perturbed [24]. The stability of solitons opened up a new method for compression of pulse using dispersion decreasing fiber [30,31].

2.3.5 Stimulated Brillouin Effect

Any physical system has a tendency to lower its energy. For an electric dipole which has potential energy related by $U = -\boldsymbol{p}.\boldsymbol{E}$ **.** The atoms are more willing to move the center of the beam since the intensity thus the electric field is higher, as shown in Figure 2.5. This effect is called electrostriction, and for a solid, it causes strain due to the higher mass density in the areas where the center of the beam is located [23].

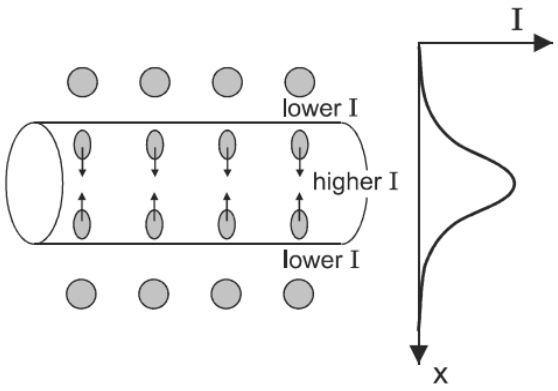

Figure 2.5 The electrostriction effect

When the light with frequency Ω_i interacts with the material, it scatters with the scattered wave frequency Ω_s . Because of the electrostriction effect, the acoustic wave with the following frequency $\Omega_a = k_a\, v_a$ is created. Using energy conservation $\Omega_i = \Omega_a + \Omega_s$ and momentum conservation $\boldsymbol{k_i = k_a + k_s}$ gives a more explicit relation for the acoustic frequency as follows

$$\Omega_a = k_a v_a = 2\, v_a\, k_i \sin\left(\frac{\theta}{2}\right) \tag{2.30}$$

Where, v_a is the acoustic wave velocity and the θ is the angle between the pump and the scattered wave vectors [22]. The magnitudes of the pump and scattered wave vectors are assumed equal. The Equation 2.3.12 indicates that stimulated Brillouin scattering is maximum in the backward direction and zero in the forward direction. The intensity of the pump and scattered waves depends on losses, initial intensities and Brillouin gain which depends on material and frequency. Threshold power is directly proportional to gain, length and inversely proportional to area. Similar to the lasing threshold when the threshold power is exceeded, spontaneous Brillouin scattering becomes stimulated and the intensity of the scattered wave increases exponentially due to positive feedback [22].

2.3.6 Stimulated Raman Scattering

When light with frequency Ω_i propagates in silica fiber, it scatters from the silica molecules with the scattering frequency Ω_s . As a result, silica molecules are excited to a higher vibrational energy state equal to the energy difference between the incident and the scattering wave energy as shown in Figure 2.6. Raman frequency shift can be calculated from energy conservation which equals to $\Omega_r = \Omega_i - \Omega_s$. Unlike Brillouin scattering, Raman scattering occurs in both forward and backward direction [22].

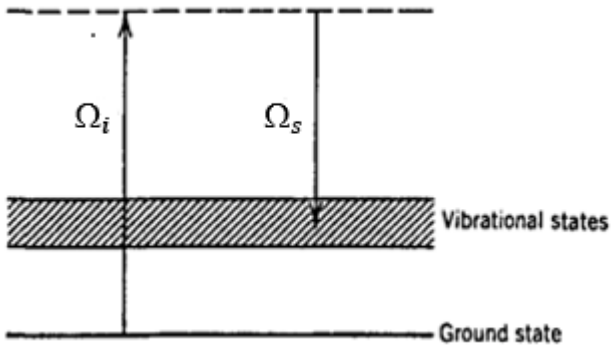

Figure 2.6 Raman Scattering

Similar to Brillouin scattering, the threshold depends on length, area and the Raman gain in a same way. After the threshold scattering wave intensity increases exponentially. The Raman gain can be used for Raman laser [32]. Another important application of Raman scattering is the Raman spectroscopy which has been used for medical purposes for a long time [33].

CHAPTER 3

EXPERIMENTAL METHOD AND SET-UP

In this section, some components such as the dispersion compensating fiber, and double clad Er/Yb co-doped gain fibers are discussed. The experimental method is explained and the setup is introduced.

3.1 Dispersion Compensating Fiber

The most suitable way to increase the transmission distance of fiber for an initial bit rate is to set it to dispersion equal to zero. A feasible solution to this problem is introducing a new fiber with an opposite dispersion sign to SMF and a much higher dispersion value to reduce the attenuation of the fiber optic system. This fiber is called dispersion compensating fiber (DCF). It is fabricated by decreasing the core diameter and increasing the refractive index of the core. Since the mode field diameter is smaller, the effective area is also smaller thus nonlinear coefficient is much higher than SMF. The major disadvantage of DCF is coupling loss due to the difference between mode field diameters. One way to solve this problem is to place an intermediate fiber between DCF and SMF [34].

3.2 Er/Yb Gain Fiber

The power and the efficiency values of the erbium-doped fiber amplifier (EDFA) are lower than the ytterbium-doped fiber amplifier (YDFA). This is due to the smaller absorption cross section and the lower doping concentration of erbium ions than the ytterbium ions due to clustering effect [35]. A convenient method to solve this problem is co-doping the erbium with the ytterbium ions. Ytterbium ions first absorb

the energy and then send their energy to erbium ions. One disadvantage of co-doping is high ASE at 1030 nm which restricts the output power [36].

3.3 Double Clad fiber

The difference between the double clad fiber and the single clad step-index fiber is that the double-clad fiber has outer cladding, which has a lower refractive index than inner cladding. A single mode pump diode cannot provide power as much as multimode pump diode however the beam quality is much higher than the multimode pump diode. The low beam quality light that emitted by multimode pump diode couples to the inner cladding with a high coupling efficiency due to a large area. Therefore, the higher output power is obtained and the pump light experiences total internal reflection between inner and outer cladding. In the doped core, stimulated emission occurs which amplifies the signal. Generally, double clad geometry is used with Er/Yb co-doped gain fibers [37].

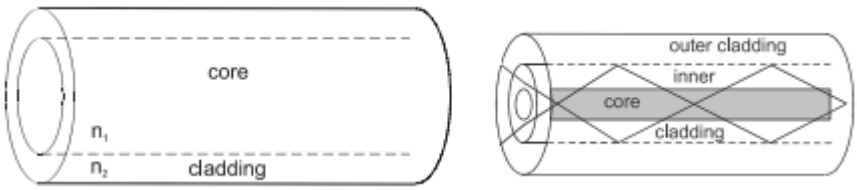

(a) (b)

Figure 3.1 Configuration of a (a) single clad fiber (b) double clad fiber

3.4 Experimental Method

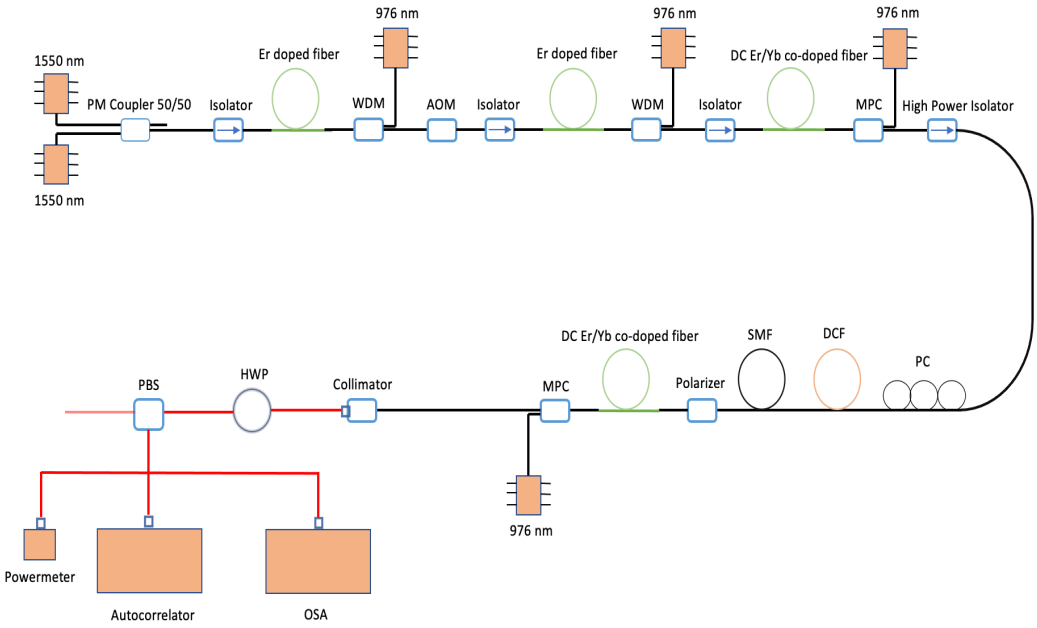

Figure 3.2 The experimental setup

Two continuous diode lasers are connected to the laser drivers which can adjust the wavelength by changing the temperature. One of the laser diodes is fixed in wavelength, the other one is changed to a specific wavelength such that the desired repetition rate is obtained with the following relation $\Delta v = \frac{c}{\lambda^2}\Delta\lambda$. These two beams are combined by polarization maintaining coupler. DCF is used as a nonlinear medium since its effective area is much smaller than the SMF hence nonlinear coefficient is much higher. There are three amplifiers and an acousto-optic modulator (AOM) in order to increase the peak power for higher four-wave mixing efficiency. The final amplifier is placed for compensating the loss due to DCF and polarizer.

CHAPTER 4

CHARACTERIZATON OF EXPERIMENTAL SETUP

In this chapter, the experimental setup was characterized cumulatively by dividing it into parts. The spectrum, power and pulse duration were analyzed in each part.

4.1 Seed Lasers and Coupler

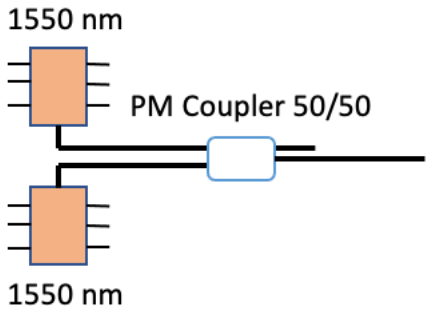

Figure 4.1 Two continuous-wave seed diodes and PM coupler

The experimental setup starts with two single-mode laser diodes (QDFBLD-1550-100NN) at 1550 nm with 100 kHz spectral width and wavelength temperature tunability and wavelength current coefficients 0.1nm/C° and 2-4 pm/mA respectively. These laser diodes are type 2 which is compatible with the laser driver (Thorlabs CLD105). The temperature stability of the drivers is close to 0.005 C° which corresponds to a 0.5 pm difference in wavelength and a 140 MHz difference

in repetition rate. The drivers control the temperature and current of the diodes with high precision and accuracy which is very important for adjusting the repetition rates. Laser diodes have polarization maintaining (PM) fiber pigtail that spliced to PM coupler (50/50) with commercial Fujikura splicer at panda mode. Other than this coupler and seed diodes, only the polarizer in this setup has PM fiber rest of the components are non-PM. Combining these two continuous waves with PM fiber is crucial for generating a beat pulse efficiently. Seed laser 1(2) was fixed in terms of temperature and current with values 35C° (23.07C°) and 440mA (355mA) respectively. When only seed laser 1(2) is operating, the power at the output of the 50/50 coupler is 36.88mW (36.83mW) and the wavelength is 1546.522nm (1546.402nm).

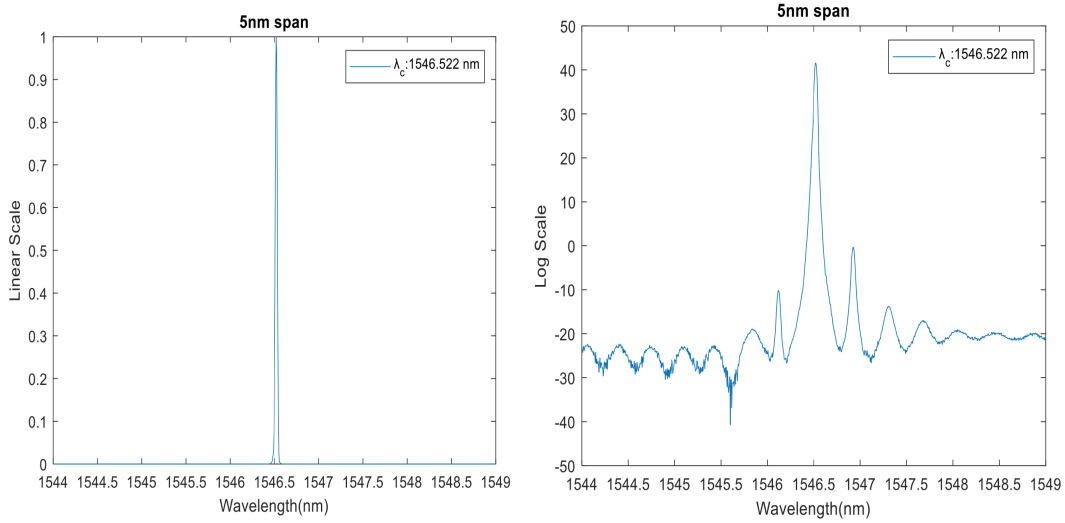

(a) (b)

Figure 4.2 The spectrum of the seed diode 1 after the PM coupler at 35 C°, 440 mA and 36.88 mW (a) in linear scale (b) in log scale

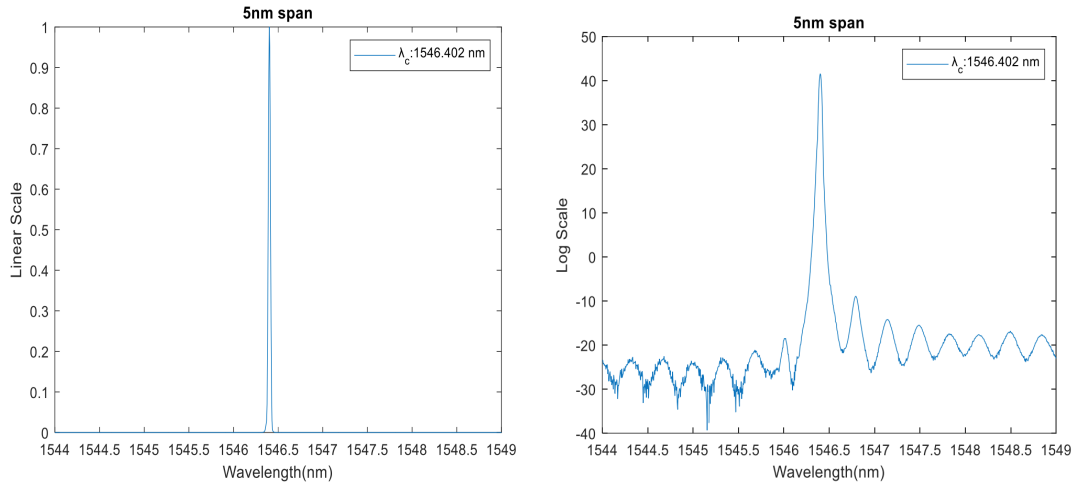

(a) (b)

Figure 4.3 The spectrum of the seed diode 2 after the PM coupler at 23.07 C°, 355mA and 36.83 mW (a) in linear scale (b) in log scale

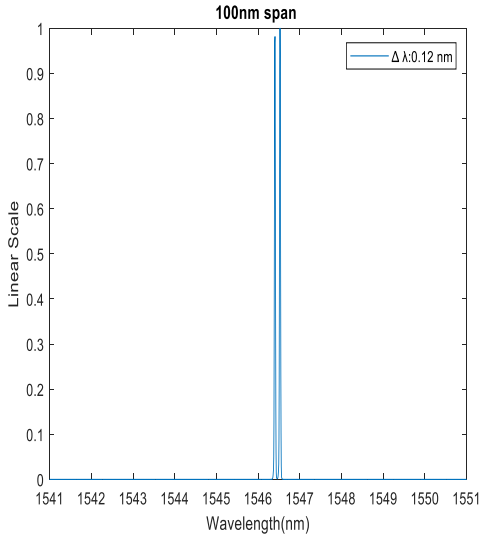

Figure 4.4 The spectrum of the beat pulse after the PM coupler

By changing the temperature of the seed diode 2, the wavelength difference hence the repetition rate can be adjusted. Equating the powers of both seed diodes is essential for low background signal. Normally changing the temperature varies the output power of the seed diodes, however changing a few GHz repetition rate corresponds to a temperature difference much lower 1C°. Therefore, power variation due to temperature can be neglected. Rest of the results the repetition rate was kept at 15 GHz (0.12nm) as shown in Figure 4.4.

4.2 First Amplifier and Acousto-Optic Modulator

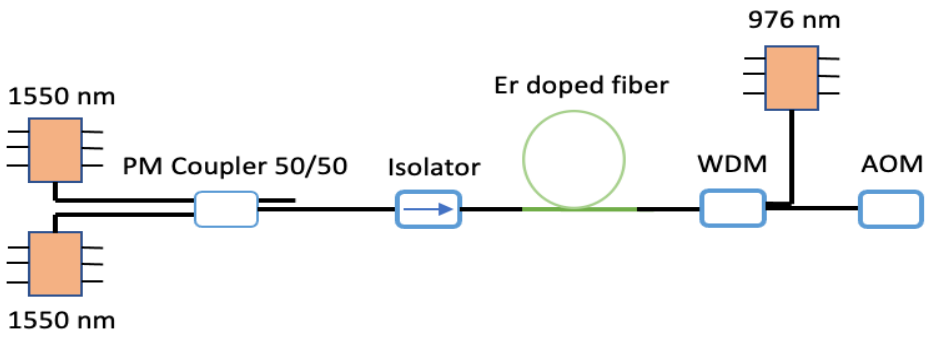

Figure 4.5 EDFA and the AOM were included to the experimental setup

After the PM coupler, the seed signal with a repetition rate of 15 GHz and power at ≈73 mW was amplified by erbium doped fiber amplifier (EDFA). All of the amplifiers in this setup were backward pumped due to higher efficiency than forward pumping [38]. First EDFA consists of a single mode pump diode at 976 nm, wavelength division multiplexing (WDM) for both pump and signal to propagate, 84 cm-long Er-80 8/125 fiber and isolator. The isolator prevents possible damage that can be induced by back reflection and ASE.

After the first amplifier, the continuous wave signal is modulated by the AOM. The AOM is connected to a function generator which generates pulses with the duration 40 ns and 100 kHz repetition rate. The duty cycle of pulses is 0.4%. Insertion loss and the low duty cycle reduced the average power to 172 µW. The advantage of adding AOM on setup is boosting the peak power, as a consequence the efficiency of four-wave mixing is increased. Although decreasing repetition rate increases burst pulse energy after the further amplification which is determining parameter such as for material processing, at low repetition rate values the ASE becomes more significant [39]. The pump diode was kept at a maximum current which is 650 mA. At 650 mA, the output power was 141.7 mW then it reduced to 172 µW after the AOM.

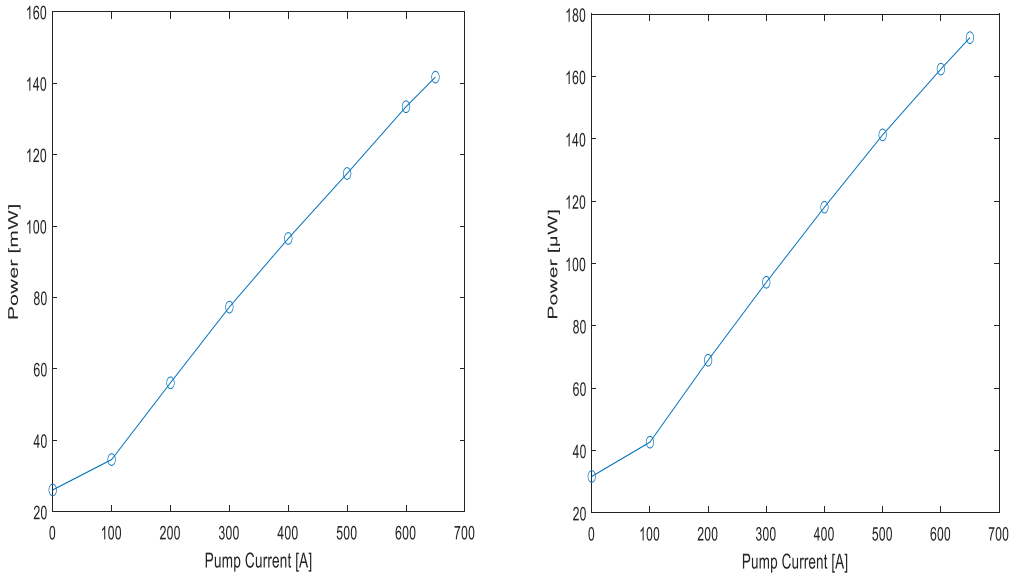

(a) (b)

Figure 4.6 The output power and the pump current values (a) before the AOM (b) after the AOM

4.3 Second Amplifier

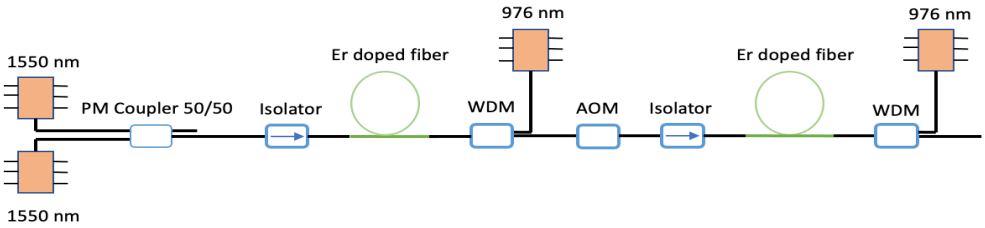

Figure 4.7 The second EDFA was included to the experimental setup

Second EDFA is added before the erbium-ytterbium co-doped fiber amplifier (EYDFA) due to the large possible ASE content because of the high gain amplification of a low signal. The difference between the first and second amplifiers is the gain fiber. The gain fiber in the second EDFA is 1 m-long Er-40 4/125. The bump on the left side of the spectrum is ASE as shown in Figure 4.7. Since ASE increases with the power and it is amplified after each amplifier stage, the pump current was kept at 200 mA before the EYDFA. After the AOM, the signal was amplified to average and peak power of 13.53 mW and 3.38 W respectively. Moreover, the mode field diameter of this erbium doped fiber is 4 µm which is half of the first gain fiber. Hence, the nonlinear coefficient is approximately four times higher. Therefore, the first sidebands of FWM popped up as can be seen in Figure 4.8.

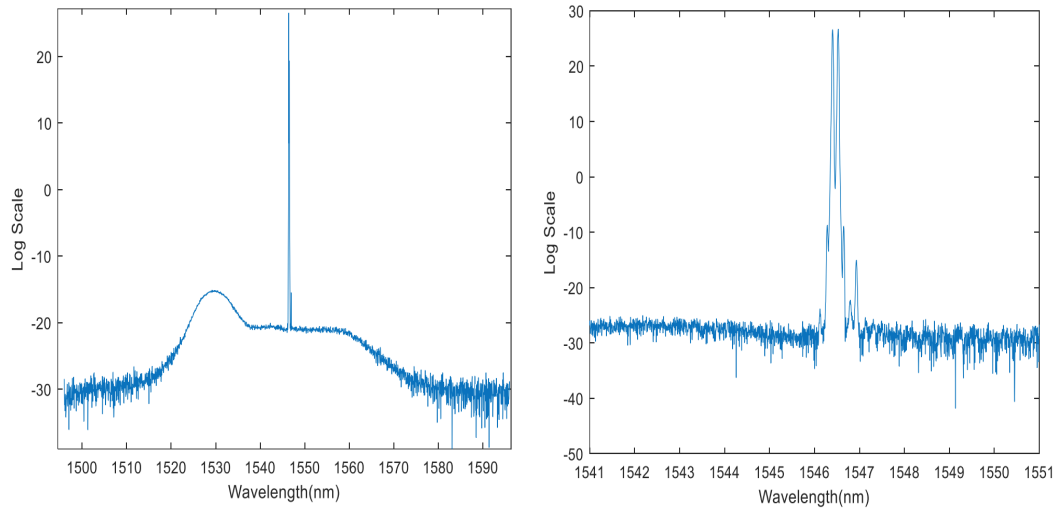

(a) (b)

Figure 4.8 The spectrum after the second EDFA (a) spanning 100 nm (b) spanning 10 nm

4.4 Third Amplifier, Polarization Controller

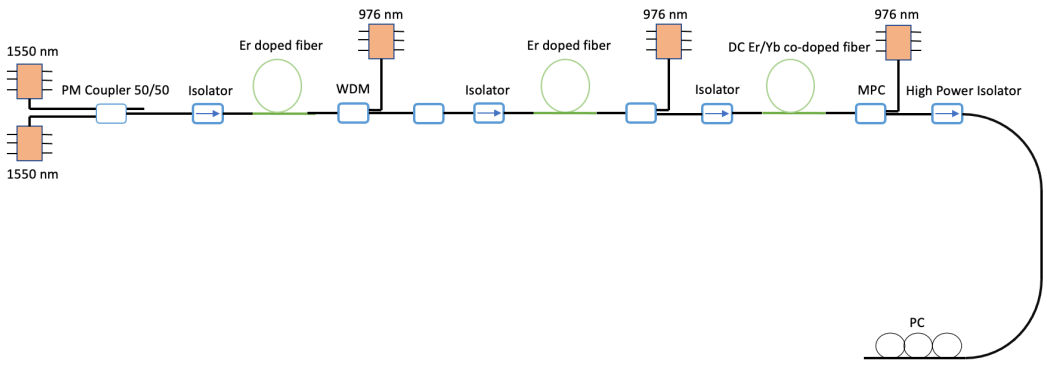

Figure 4.9 EYDFA and the polarization controller (PC) were included to the experimental setup

It is necessary to add a third amplifier so that power reaches the optimum level for the most efficient FWM product. Instead of WDM in the first two amplifiers, a multimode pump combiner was used for combining signal and pump. Another difference between the first two amplifiers is the cladding pump. Here, the gain fiber is a double-clad Er/Yb co-doped fiber with the length of $2.4\ m$.

After the third amplifier, a polarization controller was added to the experimental setup due to the dependence of the four-wave mixing process on polarization. The polarization controller has a bending loss which is approximately %26.

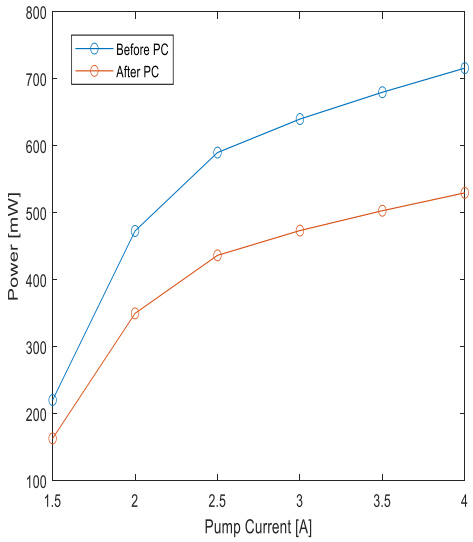

Figure 4.10 The pump current and the power values before and after the PC

4.5 Dispersion Compensating Fiber and Single Mode Fiber

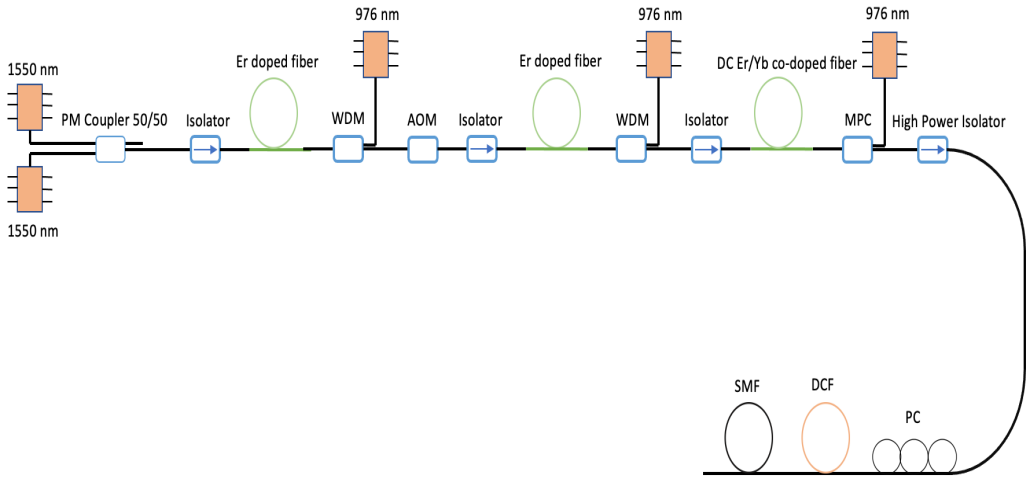

Figure 4.11 DCF and SMF were included to the experimental setup

DCF with dispersion coefficient $-140\frac{\text{ps}}{\text{nm.km}}$ was used as a nonlinear medium where FMW occurs. Since the nonlinear effects other than FMW such as Raman scattering also depend on the power and the length of the DCF, the third amplifier's pump current can be determined after adding the DCF. The mode field diameter of DCF and SMF-28 is 5 μm and 10 μm respectively. Because of huge variations in mode field diameter between SMF and DCF, the coupling loss is enormous. Besides placing an intermediate fiber to reduce the loss, adjusting the splice parameters such as arc power and time decreased the loss from %69 to %41. Power and bandwidth characteristics after the various lengths of DCF are shown by the following figures

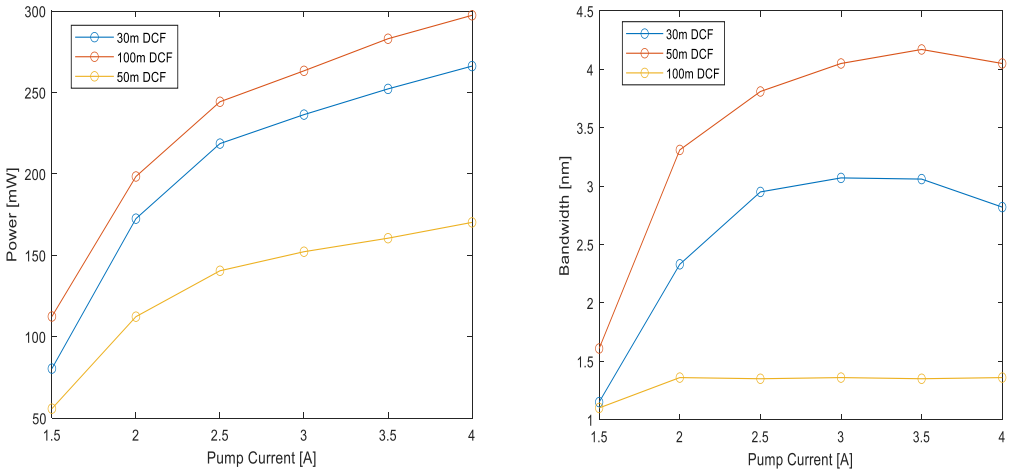

(a) (b)

Figure 4.12 (a) The pump current and the output average power values of 30m,50m,100m long DCF (b) The pump current and the bandwidth values of 30m,50,100m long DCF

Pulse duration and bandwidth are inversely proportional to each other. 50m DCF corresponds to the shortest possible duration compared the 100m and 30m because of the higher bandwidth. The lowest bandwidth values appeared with 100m DCF. This is mainly because of the balance between FWM and Raman scattering. The spectrums after the 100m DCF with pump current at 1.5A and 2A are shown in the following figures

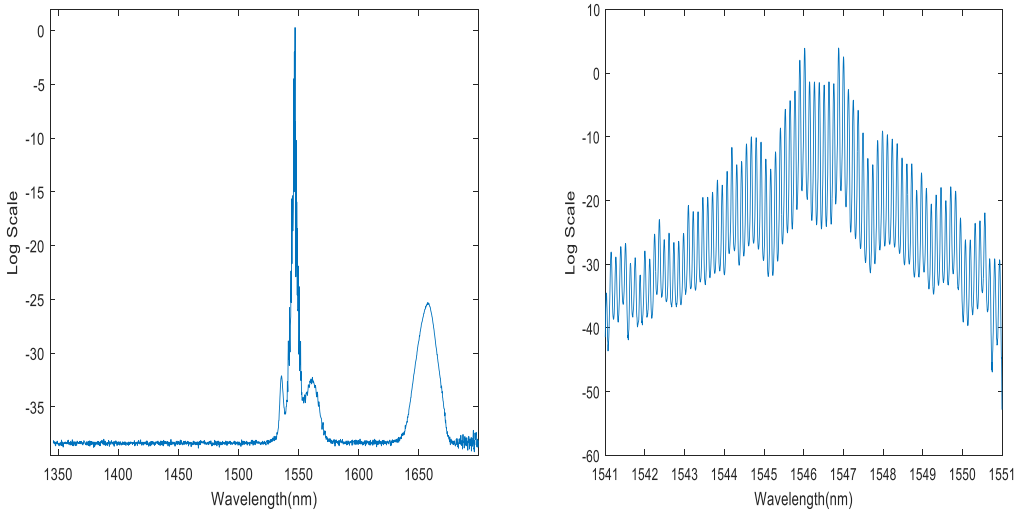

(a) (b)

Figure 4.13 The spectrum after the 100 m long DCF at average power of 111.2 mW (a) spanning 100 nm in log scale (b) spanning 10 nm in log scale

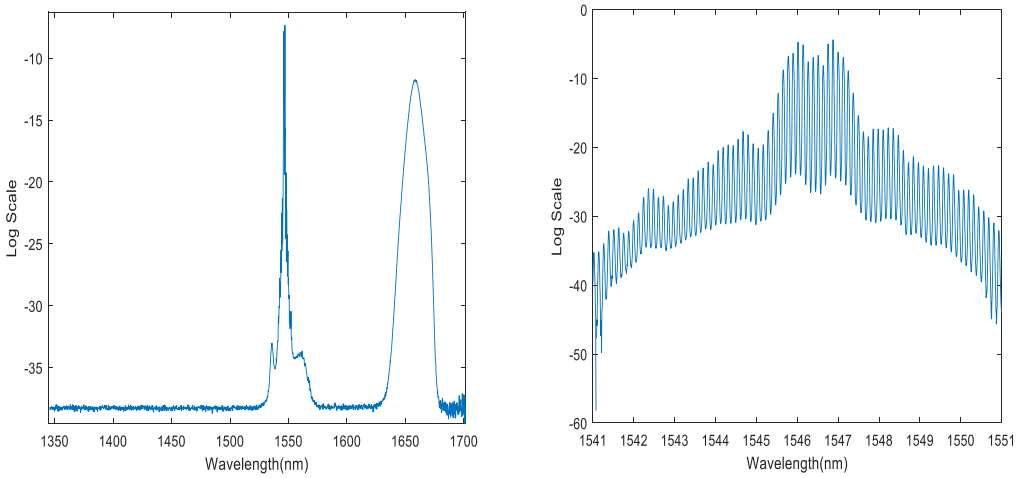

(a) (b)

Figure 4.14 The spectrum after the 100 m long DCF at average power of 198.4 mW (a) spanning 100nm in log scale (b) spanning 10nm in log scale

The Raman gain depends on the frequency shift which is approximately 13.1 THz and the gain is $6x10^{-4}m/W$ [23]. The second peak in Figures 4.13 and 4.14 is around at 1657 nm and the difference between the laser wavelength is 110nm which is close the 13.1 THz. Therefore, the second peak corresponds to Raman scattering. While input power increases, the Raman peak rises since more power means higher intensity thus more photons are scattered. As DCF length goes up both FMW and Raman scattering effects also increase. The bandwidth increases due to the FMW process and the Raman scattering disrupts the spectral phase thus declining the efficiency of FMW hence decreasing the bandwidth.

When there is no chirp, the product of pulse duration and bandwidth is at the lowest level. Since DCF induces positive dispersion, standard SMF-28 with negative dispersion is added for decreasing the chirp hence it further compresses the pulse and increases bandwidth. Adding 100m SMF after the 50m DCF gives the highest bandwidth values. At 2.5A, the bandwidth is at a maximum which is 4.68nm with outpower average power 135.2 mW and a peak power 33.8 W.

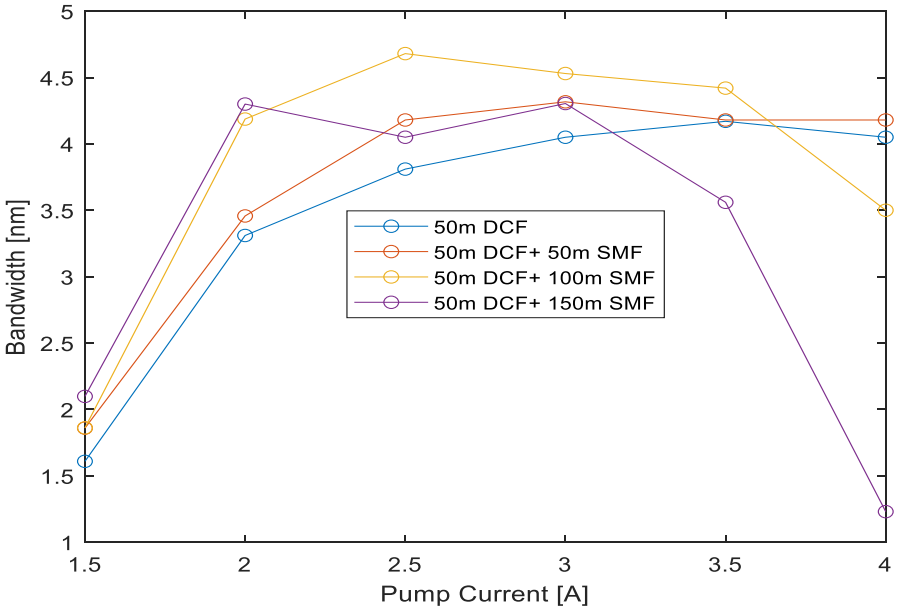

Figure 4.15 The pump current and the bandwidth values after 0m,50m,100m,150m long SMF and 50 m long DCF

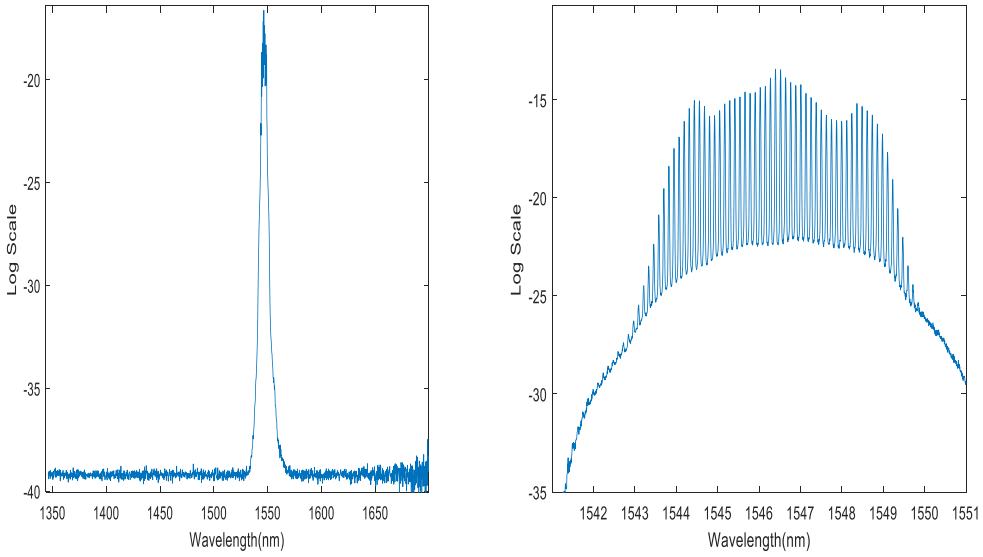

(a) (b)

Figure 4.16 The spectrum after 50 m long DCF and 100 m long SMF at 2.5A pump current with 135.2 mW average power (a) spanning 100 nm in log scale (b) spanning 10 nm in log scale

4.6 Polarizer , Final amplifier and Collimator

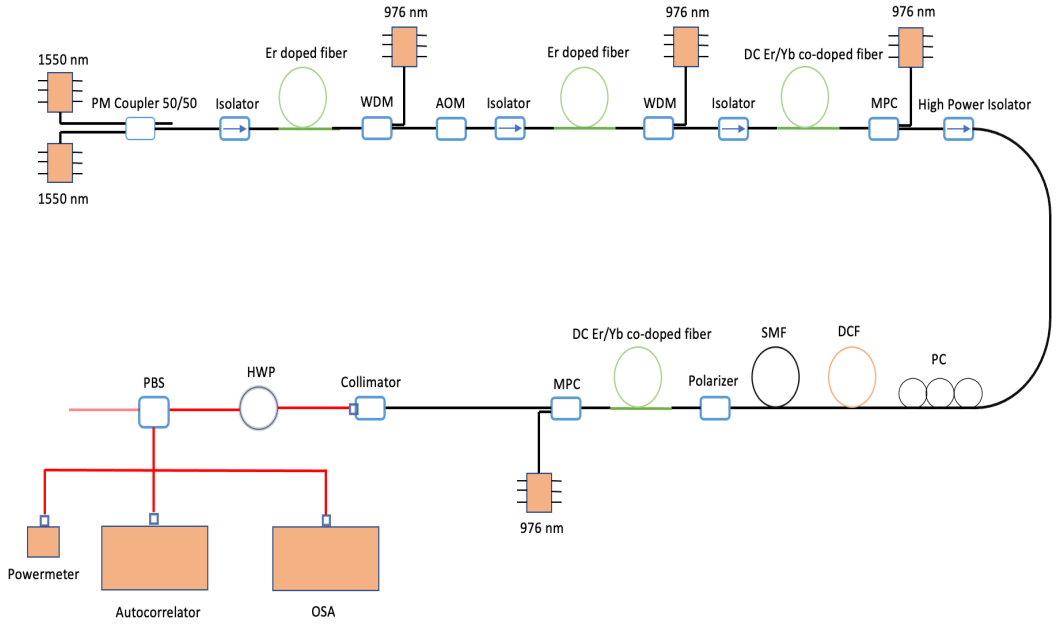

Figure 4.17 The final configuration of the experiment setup

After 100m SMF , a polarizer was placed into the experimental setup. Due to the PC and the polarizer, changing the polarization with the PC varies the power after the polarizer. The final amplifier which is the same as the third amplifier was added in order to boost the power for material processing applications. The final component of the system is the collimator which restricts the pump current of the final amplifier because of the maximum power that can handle is around 500 mW. Polarization beam splitter (PBS) and half waveplate (HWP) further control the power and polarization of the output signal which was characterized by the powermeter, autocorrelator and optical spectrum analyzer (OSA) with respect to different repetition rates and powers as following figures

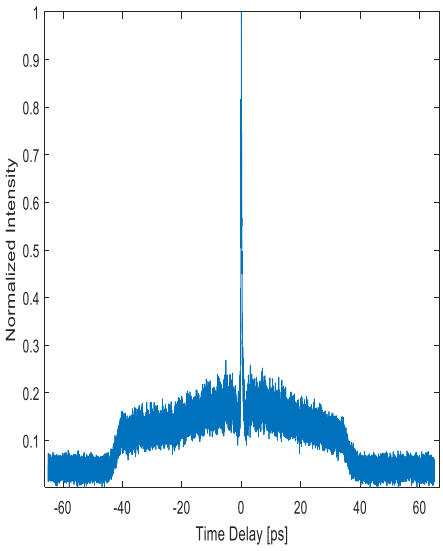
Normalized Intensity
Time Delay [ps]

(a)

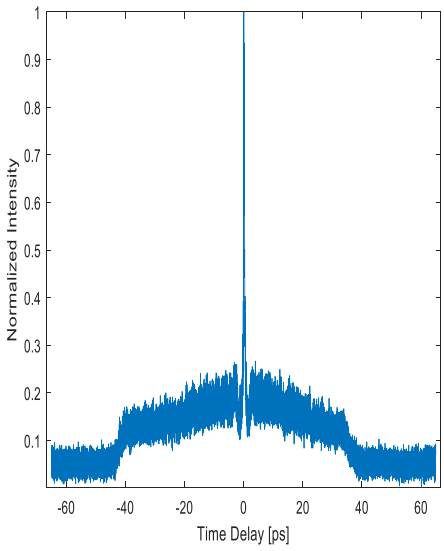
Normalized Intensity
Time Delay [ps]

(b)

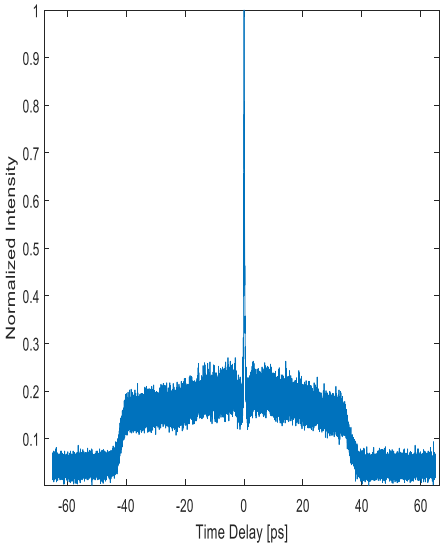
Normalized Intensity
Time Delay [ps]

(c)

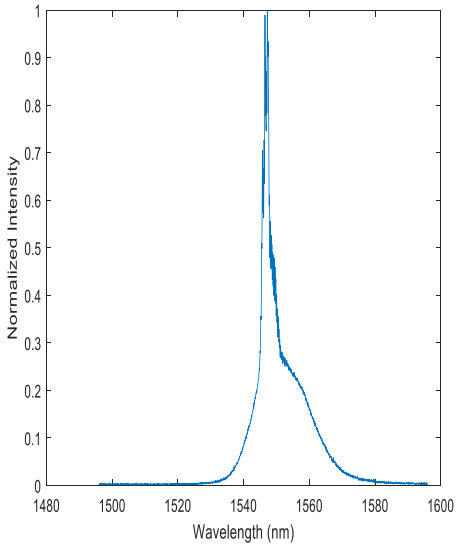
Normalized Intensity
Wavelength (nm)

(d)

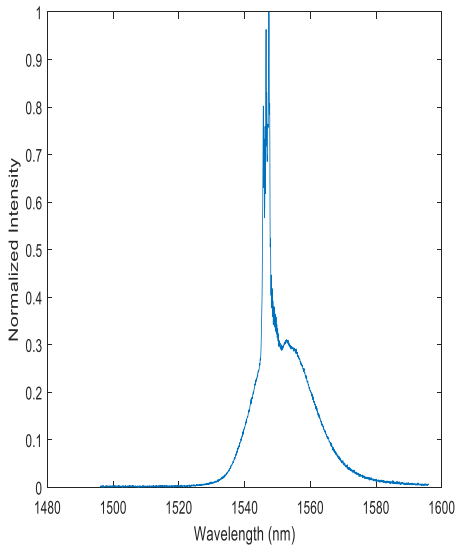

(e)

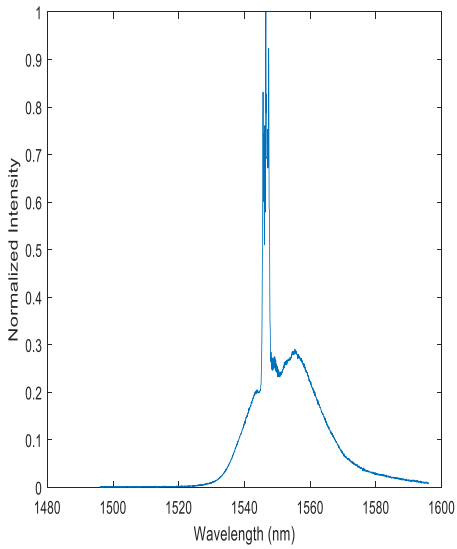

(f)

Figure 4.18 Normalized autocorrelation trace and spectrum of the 5 GHz pulses with pump current at 1.4 A, 1.6 A, 1.8 A respectively with pulse duration and bandwidth values (a) 282 fs , 59.1 mW (b) 299 fs , 90.3 mW (c) 254 fs , 139 mW (d) 3.13 nm, 59.1 mW (e) 2.5 nm, 90.3 mW (f) 2.19 nm, 139 mW

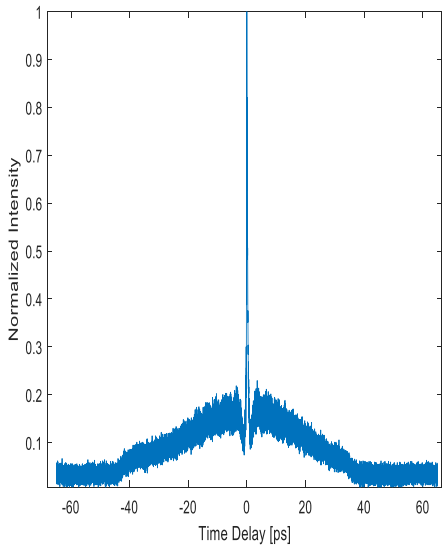

(a)

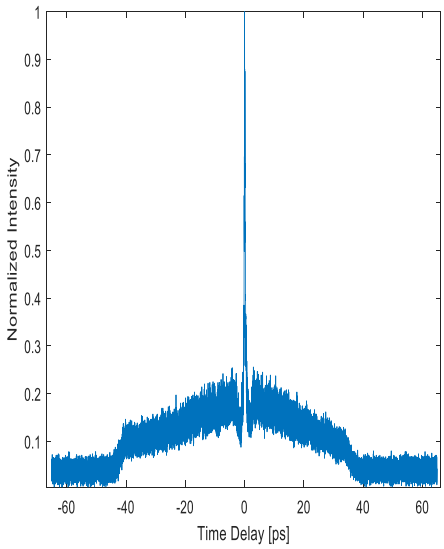

(b)

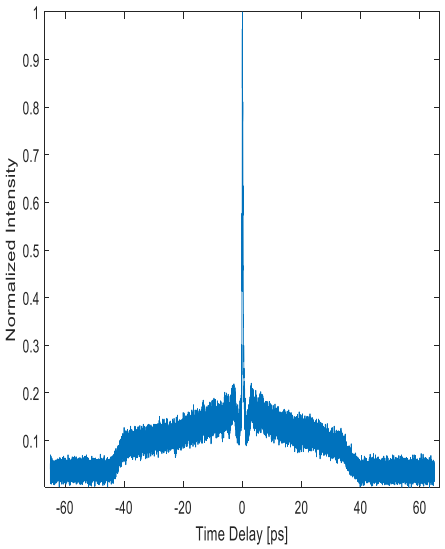

(c)

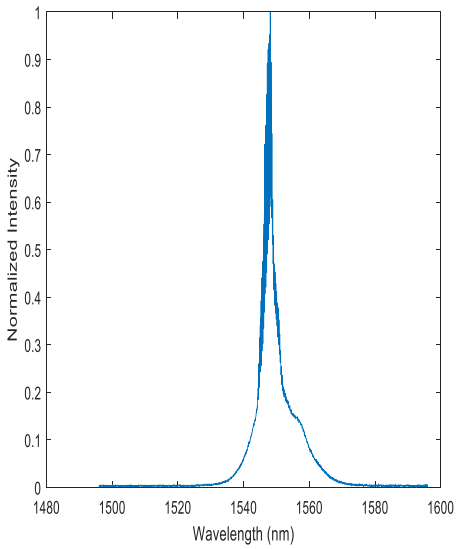

(d)

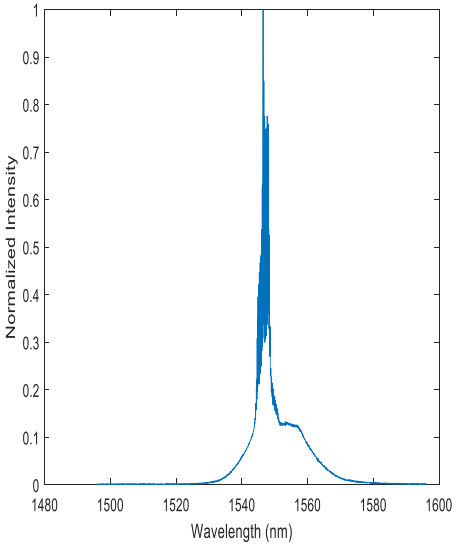

(e)

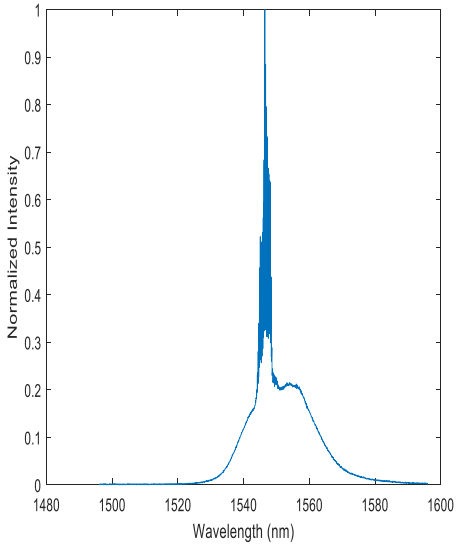

(f)

Figure 4.19 Normalized autocorrelation trace and spectrum of the 10 GHz pulses with pump current at 1.4 A, 1.6 A, 1.8 A respectively with pulse duration and bandwidth values (a) 289 fs , 39.4 mW (b) 298 fs , 63.3 mW (c) 280 fs , 119 mW (d) 3.08 nm, 39.4 mW (e) 2.31 nm, 63.3 mW (f) 3.08 nm, 119 mW

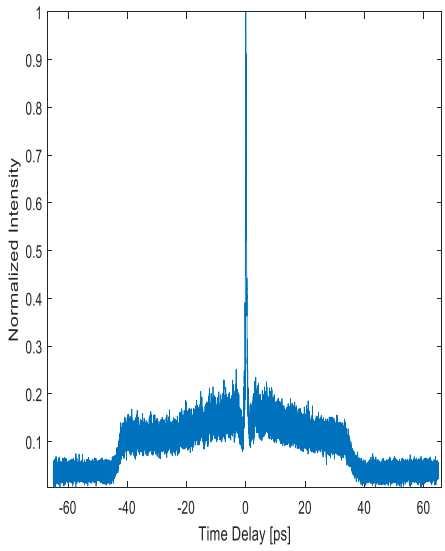
Normalized Intensity
Time Delay [ps]

(a)

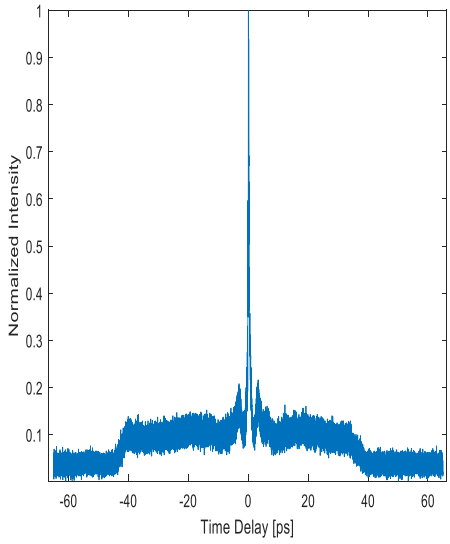
Normalized Intensity
Time Delay [ps]

(b)

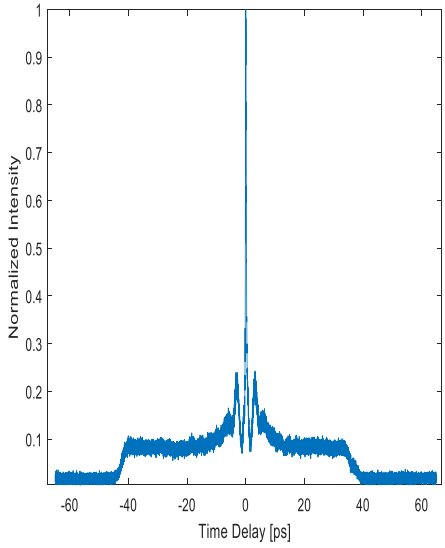
Normalized Intensity
Time Delay [ps]

(c)

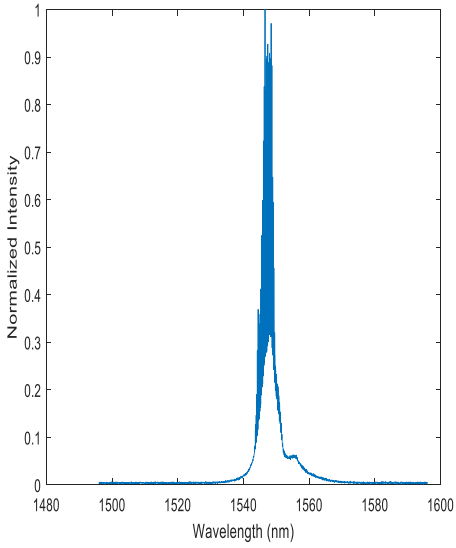
Normalized Intensity
Wavelength (nm)

(d)

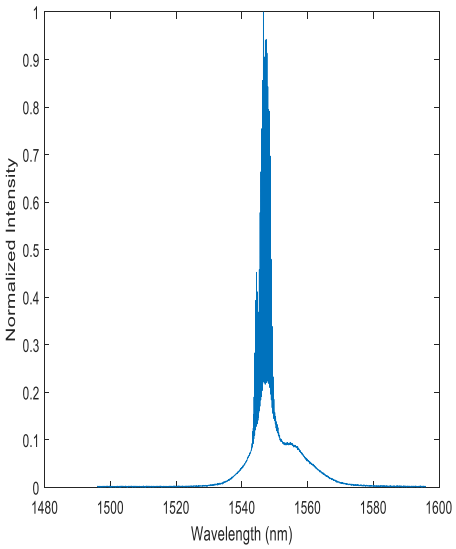

(e)

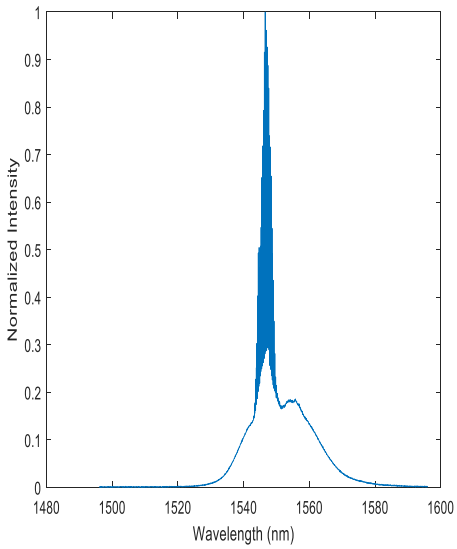

(f)

Figure 4.20 Normalized autocorrelation trace and spectrum of the 15 GHz pulses with pump current at 1.4 A, 1.6 A, 1.8 A respectively with pulse duration and bandwidth values (a) 327 fs , 26 mW (b) 305 fs , 60.5 mW (c) 282 fs , 113 mW (d) 3.48 nm, 26 mW (e) 3.13 nm, 60.5 mW (f) 3.96 nm, 113 mW

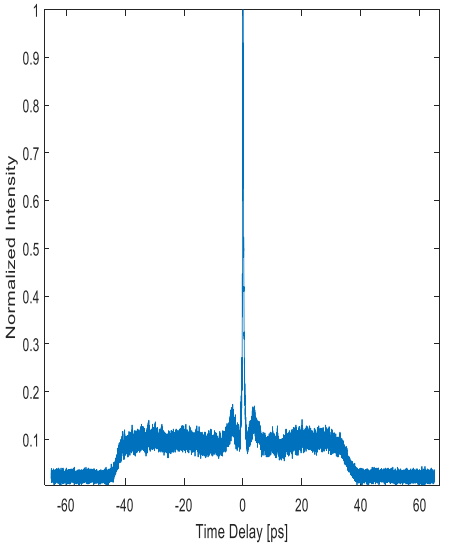

(a)

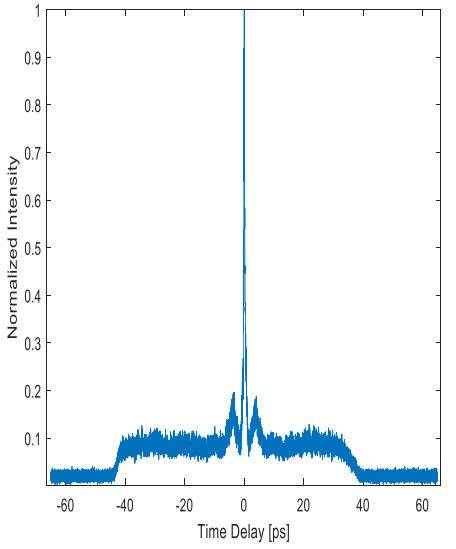

(b)

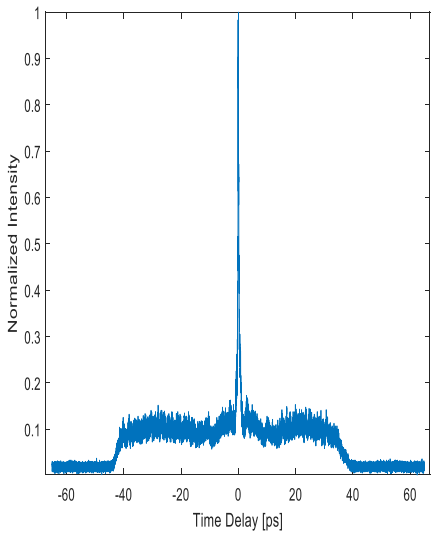

(c)

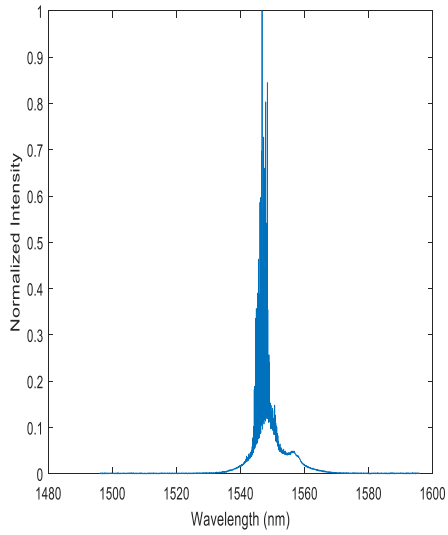

(d)

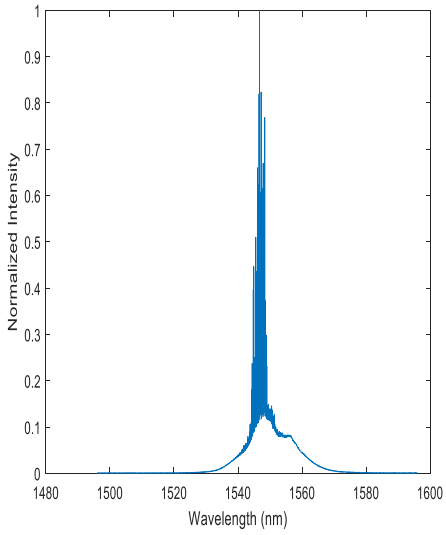

(e)

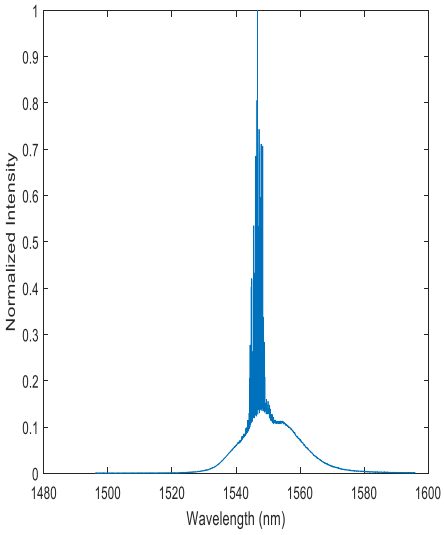

(f)

Figure 4.21 Normalized autocorrelation trace and spectrum of the 20 GHz pulses with pump current at 1.4 A, 1.6 A, 1.8 A respectively with pulse duration and bandwidth values (a) 324 fs , 39.6 mW (b) 313 fs , 80 mW (c) 249 fs , 124.2 mW (d) 2.33 nm, 39.6 mW (e) 2.82 nm, 80 mW (f) 3.02 nm, 124.2 mW

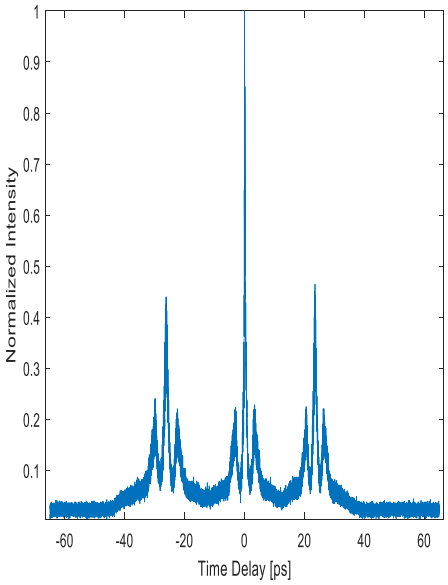
Normalized Intensity
Time Delay [ps]

(a)

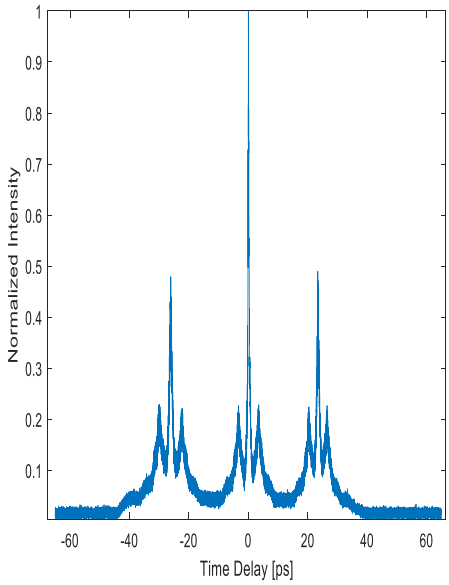
Normalized Intensity
Time Delay [ps]

(b)

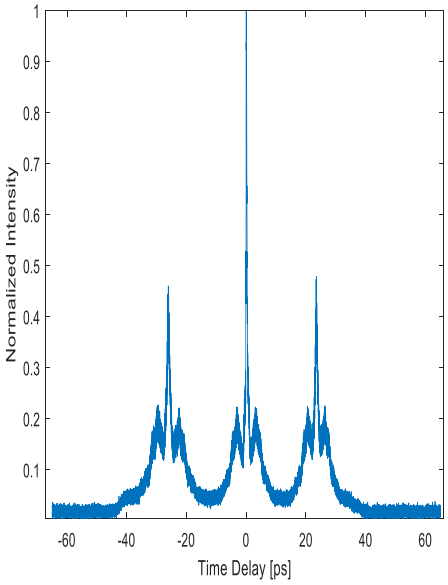
Normalized Intensity
Time Delay [ps]

(c)

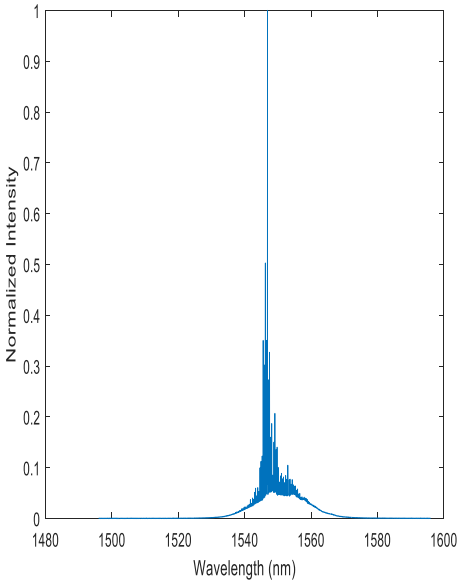
Normalized Intensity
Wavelength (nm)

(d)

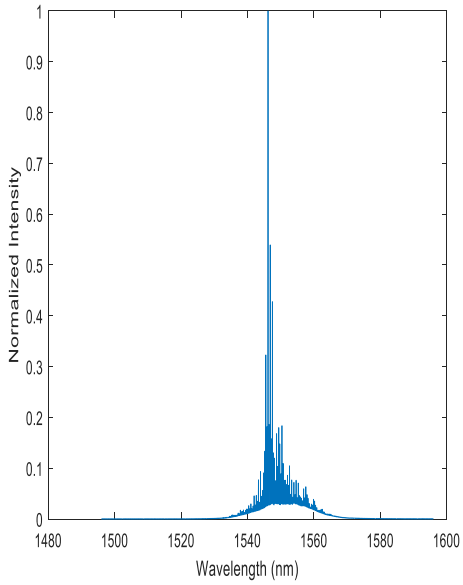

(e)

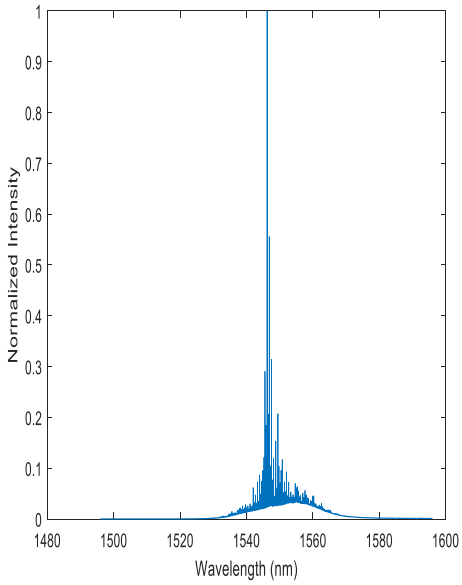

(f)

Figure 4.22 Normalized autocorrelation trace and spectrum of the 40 GHz pulses with pump current at 1.4 A, 1.6 A, 1.8 A respectively with pulse duration and bandwidth values (a) 296 fs , 80.8 mW (b) 303 fs , 124.5 mW (c) 309 fs , 179 mW (d) 0.68 nm, 80.8 mW (e) 0.67 nm, 124.5 mW (f) 0.68 nm, 179 mW

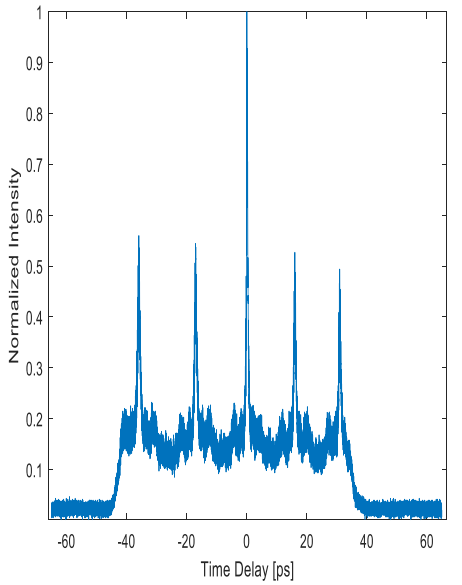

(a)

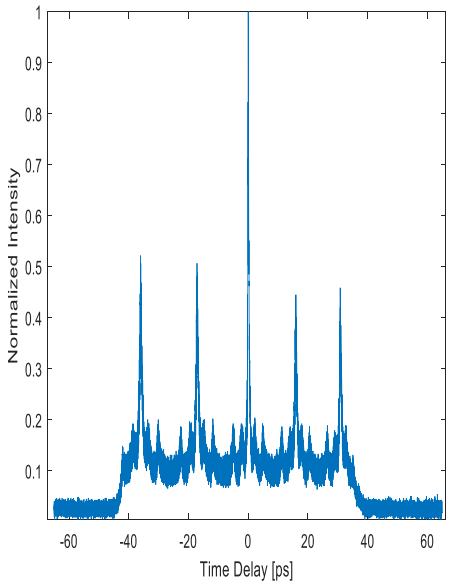

(b)

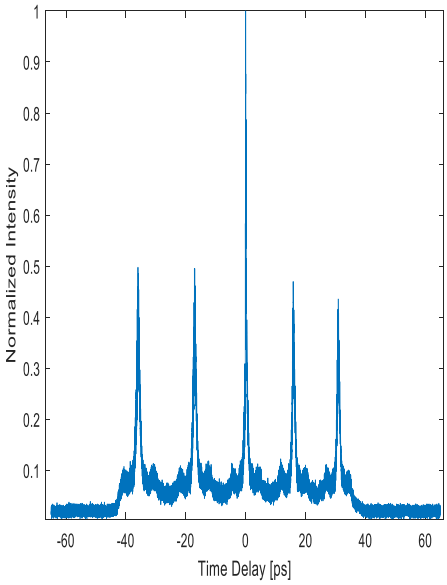

(b)

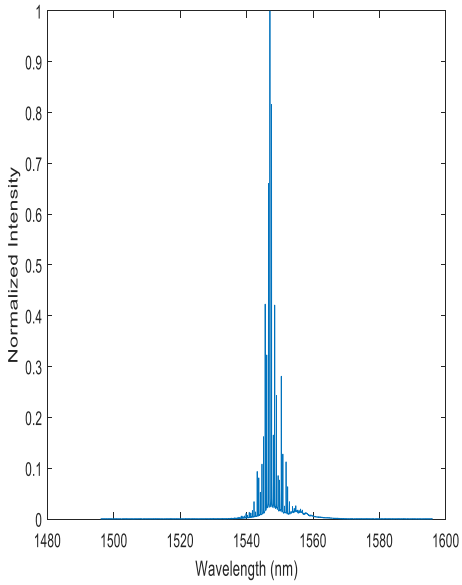

(c)

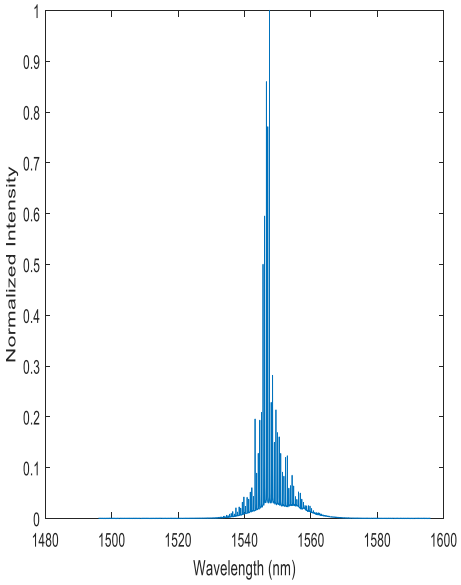

(e)

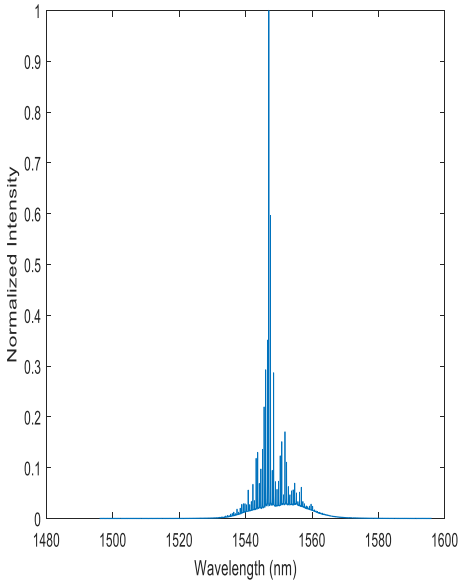

(f)

Figure 4.23 Normalized autocorrelation trace and spectrum of the 60 GHz pulses with pump current at 1.4 A, 1.6 A, 1.8 A respectively with pulse duration and bandwidth values (a) 400 fs , 37.1 mW (b) 297 fs , 71.2 mW (c) 282 fs , 124 mW (d) 0.98 nm, 37.1 mW (e) 1.97 nm, 71.2 mW (f) 0.53 nm, 124 mW

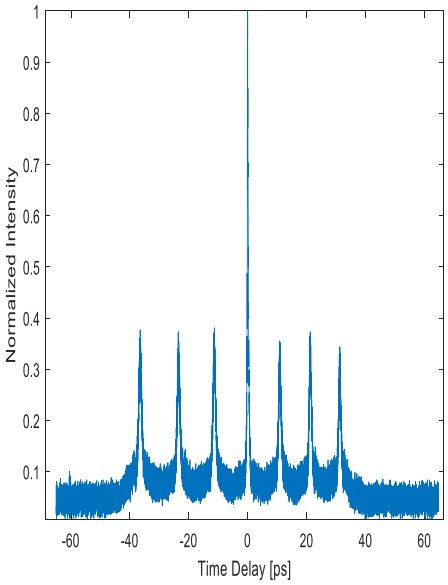
Normalized Intensity
Time Delay [ps]

(a)

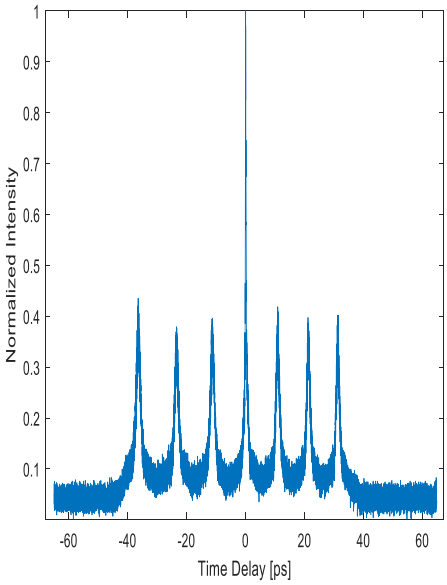
Normalized Intensity
Time Delay [ps]

(b)

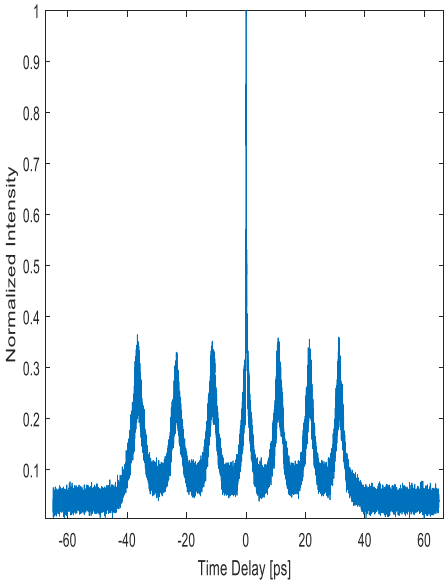
Normalized Intensity
Time Delay [ps]

(c)

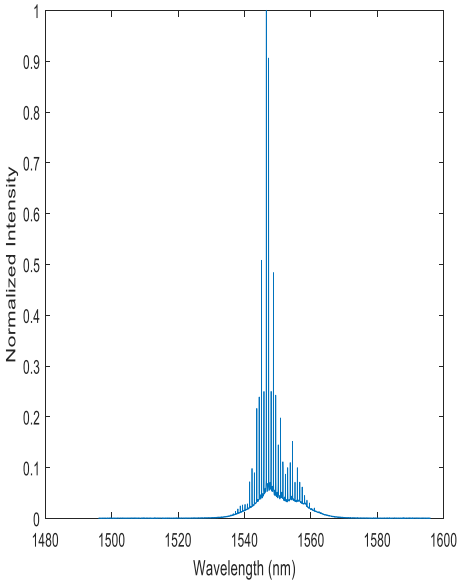
Normalized Intensity
Wavelength (nm)

(d)

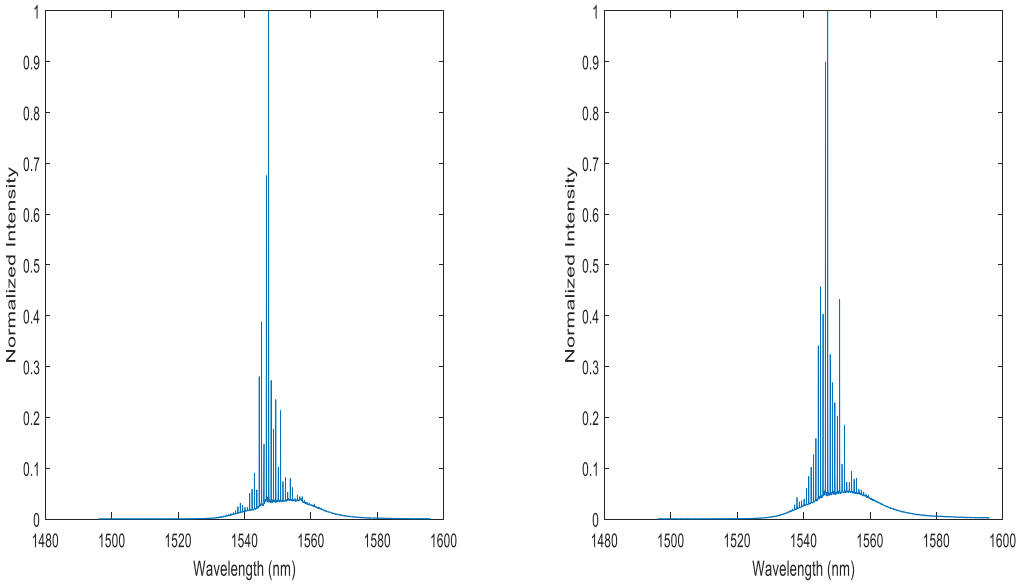

(e) (f)

Figure 4.24 Normalized autocorrelation trace and spectrum of the 80 GHz pulses with pump current at 1.4 A, 1.6 A, 1.8 A respectively with pulse duration and bandwidth values (a) 289 fs , 61.1mW (b) 275 fs , 100 mW (c) 259 fs , 154 mW (d) 2.18 nm, 61.1 mW (e) 0.74 nm, 100 mW (f) 0.75 nm, 154 mW

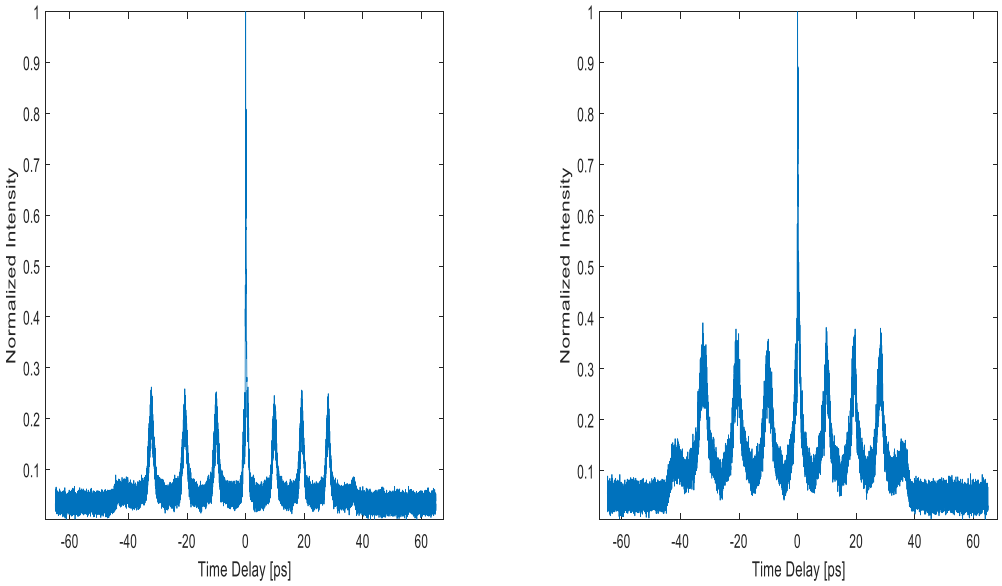

(a) (b)

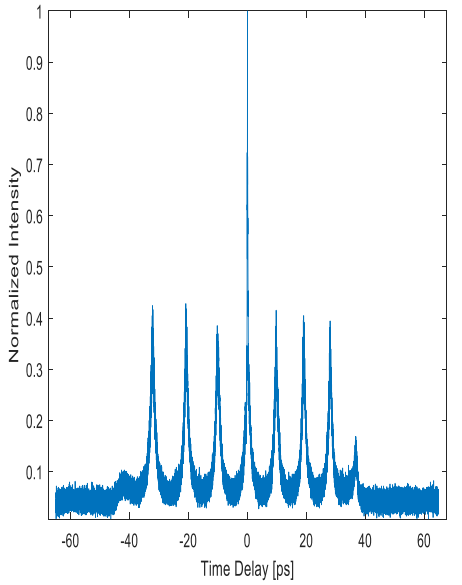

(c)

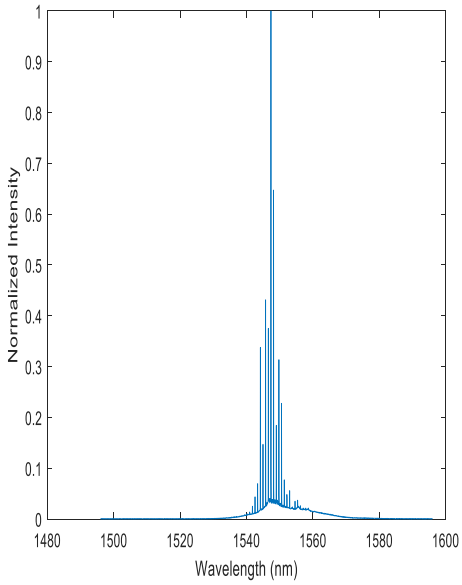

(d)

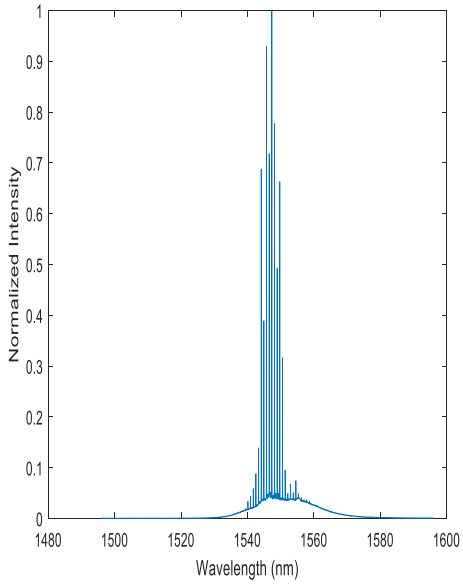

(e)

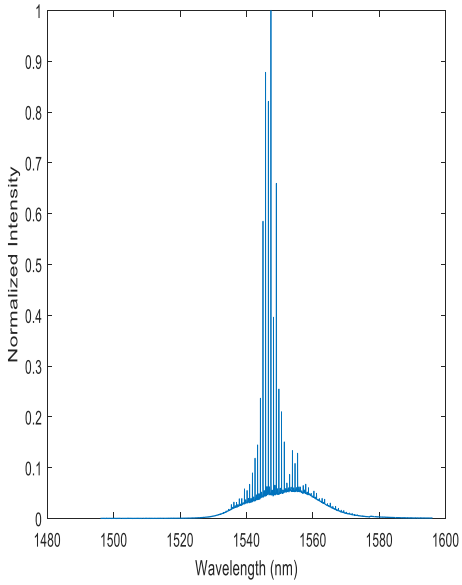

(f)

Figure 4.25 Normalized autocorrelation trace and spectrum of the 100 GHz pulses with pump current at 1.4 A, 1.6 A, 1.8 A respectively with pulse duration and bandwidth values (a) 247 fs , 39.5 mW (b) 364 fs , 79 mW (c) 232 fs , 143 mW (d) 0.84 nm, 39.5mW (e) 5.26 nm, 79 mW (f) 4.02 nm, 143 mW

All autocorrelation figures have a low intensity pedestal . Because of the high repetition rates, the peak power becomes low for inducing second harmonic generation in the autocorrelator resulting in a pedestal [17]. However , increasing the peak power did not decrease the pedestal so this is not the case for this configuration. Another mechanism of the pedestal is that the SPM induced chirp depends on the phase of the pulse and, it is linear only in the middle portion of the pulse. Therefore, the compression occurs only in the middle portion while the pulse wings remain uncompressed and form a broad low intensity pedestal. The highest bandwidth is 5.26 nm for the case 100 GHz pulses corresponding to 669 fs transform limited pulses however measured pulse duration is 364 fs . In fact, all of the pulses have lower pulse duration than their transform limited pulse duration values. The reason is that only a small portion of the pulse energy was compressed to a femtosecond regime. Further investigation of the phase and the intensity profiles of the pulses can be analyzed by frequency resolved optical gating(FROG) [40].

In a nonlinear regime, the polarization of the light rotates with respect to intensity. This phenomenon is called nonlinear polarization rotation which is beneficial for generating pulses by passive mode locking [41]. The intensity of the pedestal is lower than the femtosecond pulses. Therefore, each time before the measurements of pulse duration, the PC and HWP were rotated in order to minimize the pedestal.

	1.4 [A]		1.6 [A]		1.8 [A]	
	R	Pulse Energy	R	Pulse Energy	R	Pulse Energy
5 GHz	0.009	26.6 pJ	0.009	42.4 pJ	0.006	46.5 pJ
10 GHz	0.021	21.3 pJ	0.020	31.8 pJ	0.22	65.4 pJ
15 GHz	0.035	15 pJ	0.037	37.3 pj	0.04	75 pJ
20 GHz	0.05	24 pJ	0.06	60 pJ	0.046	71 pJ
40 GHz	0.111	55 pJ	0.114	85 pJ	0.106	118 pJ
60 GHz	0.13	20.1 pJ	0.122	36.2 pJ	0.152	78 pJ
80 GHz	0.204	38 pJ	0.168	52 pJ	0.125	60 pJ
100 GHz	0.221	21.8 pJ	0.184	36.6 pJ	0.173	62 pJ

Table 4.1 The parameter R and the pulse energy with respect to the pump current and the repetition rate

The parameter R in Table 4.1 is the ratio of area under the full width of half maximum (FWHM) of the pulse divided by the area under one period of the pulses. Multiplying the parameter R with the pulse energy gives how much energy is contained in the femtosecond pulses. The fundamental soliton energy for 300 fs pulses calculated from Equation 2.29 is approximately 158 pJ for the $20\frac{ps^2}{km}$ which is the GVD value of SMF-28. The soliton energy is higher than the femtosecond pulse energy for all cases in Table 4.1. The fundamental soliton occurs even when the parameter N is close to 0.5 due to stability. Since the soliton energy depends on parameter N quadratically , soliton can forms even at four times lower than required pulse energy. Moreover, after the PBS some of the pulse energy has

decreased. Since the pulse energy and the pulse duration is nearly the same for all intra-burst repetition rate, we think the pulse is involved in a soliton during propagation in SMF [23]. However, further investigation of this result is still required.

CHAPTER 5

MATERIAL PROCESSING

In this chapter, laser-matter interactions were briefly discussed and as an application, the subsurface processing of silicon was demonstrated.

5.1 Laser-Matter Interactions

When the bandgap energy of the material is lower than the incident photon energy, electrons in the valence band excited to the conduction band resulting in linear absorption. The linear absorption process depends on linearly to the intensity as given by the following equation

$$\frac{dI}{dz} = -\alpha I \tag{4.2}$$

Where, α is the proportionality constant called the absorption coefficient.

For high intensity regime where nonlinear effects become signification, the equation above must include higher order terms as follows [42]

$$\frac{dI}{dz} = -\alpha I - \beta I^2 \tag{4.2}$$

Where, β is the two-photon absorption coefficient.

The bandgap energy of the silicon and corresponding wavelength values are 1.12 eV and 1.1 µm respectively. In order to process inside the silicon, the light should be in a transparent regime. In other words, the wavelength of the light must be higher than 1.1 µm. In a transparent regime, linear absorption is negligible. Therefore, absorption occurs only if the intensity of the light is large enough for two photon absorption takes place. The intensity of the light is directly proportional to pulse energy and

inversely proportional to pulse duration and spot size of the beam. Therefore, lasers with ultrashort pulse durations are more favorable due to higher intensity. Another benefit of using ultrashort laser pulses is that it decreases thermal damage and hence improves precision since the thermal diffusion constant is larger than the pulse duration especially for femtosecond lasers. Furthermore, thermal damage can be reduced by operating the laser at a high intra-burst repetition rate mode. Because of the successive high repetition pulses, there is no time to heat to dissipate away from the processing area. Although single pulse energy is not enough to process, high repetition rate pulses can process because of lack of time to cool down [43,44]. The subsurface processing of the silicon enables to generating of optical devices inside the silicon such as waveguides, microchannels, grating [45,49].

5.2 Subsurface Processing of Silicon

Double side polished, 500 μm thick, <100>, p-type silicon wafer was processed in this experiment. The silicon sample was attached to the 3D translational stage. Before the translational stage, the aspheric lens with a focal length of 8 mm was positioned in order to boost the intensity. Because of the high intensity, plasma is generated which defocuses the beam since it decreases the refractive index. Plasma defocusing effects are compensated by the self-focusing effect [50]. By changing the position of the 3D stage with respect to the beam direction, the plasma was produced on the surface which indicates the intensity is maximum at the surface.

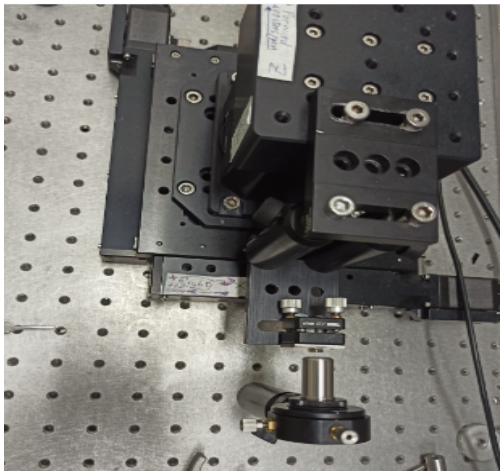

Figure 5.1 The aspheric lens and the 3D stage

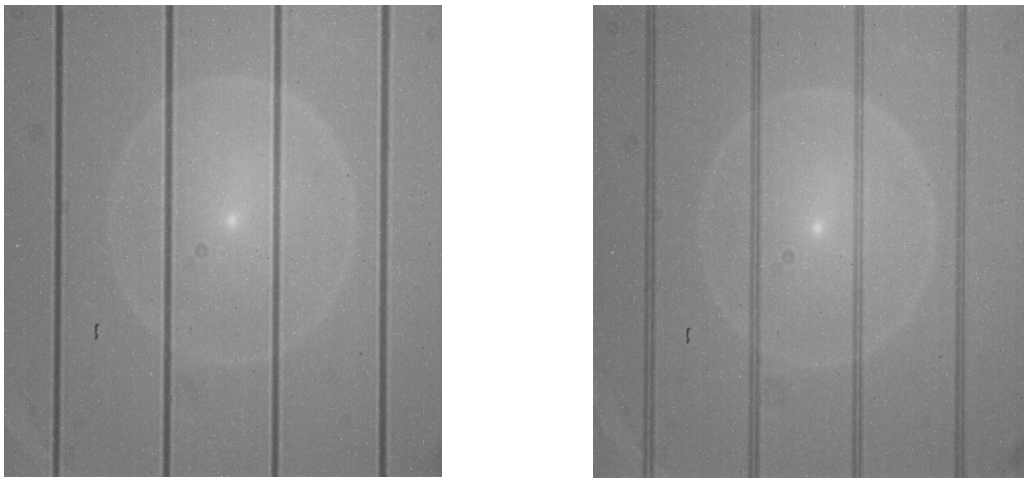

(a) (b)

Figure 5.2 Infrared microscopy images of the processed area with X40 magnification at different positions with respect to focal plane (a) away from the camera (b) closer to the camera

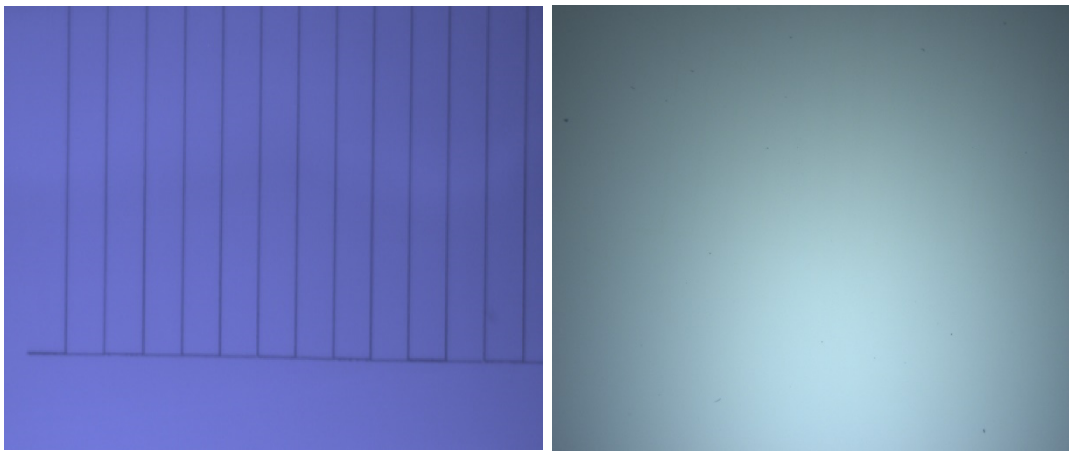

(a) (b)

Figure 5.3 (a) Infrared transmission microscopy image (b) image of the surface in the same zone

The first trial for subsurface processing was made by 20 GHz pulses with duration 249 fs, average power 124.2 mW, ratio coefficient 0.047 and pulse energy 69 pJ. However, it was not sufficient for processing. Therefore, the HWP was rotated such that pulse duration, average power and pulse energy were increased to 926 fs, 320 mW, 160 pJ with R parameter 0.04 respectively. When the silicon sample was shifted away from the focal plane toward the infrared camera, the contrast changed due to a negative refractive index difference as shown in Figure 5.2. The numerical value of the refractive index difference can be calculated by Abel transform [48]. Images in Figure 5.3 indicate that there were no any surface modifications. Therefore, the processing was occurred inside the silicon.

CHAPTER 6

CONCLUSION

In this thesis, oscillator-free femtosecond laser with high intra-burst repetition rate continuously tunable in the range between 5 GHz and 100 GHz was demonstrated. The beat pulses were broadened by the FWM inside the DCF while inducing positive chirp and then they were compressed by the negative dispersion SMF-28 fiber.

In chapter 4, the laser was constructed cumulatively from scratch. At each stage, the system was characterized in terms of power, spectrum and pulse duration while the unwanted effects such as ASE and Raman scattering were minimized. The optimum scenario occurred with the combination of a 50m-long DCF and a 100m-long SMF-28. The pedestal was created during the compression process and it was reduced by the nonlinear polarization rotation by adjusting the polarization controller and the HWP. We believe that the pulse is involved in a soliton during propagation in SMF because the pulse energy and the pulse duration did not change substantially with varying intra-burst repetition rates. As an application of this system, the subsurface of silicon was processed by 20 GHz intra-burst pulses and the processed regions exhibited negative refractive index difference.

REFERENCES

1. Einstein, A., Zur Quantentheorie der Strahlung. Physikalische Zeitschrift, 1917. 18: p. 121-128.
2. Maiman, T.H., Stimulated Optical Radiation in Ruby. Nature, 1960. 187(4736): p. 493-494.
3. F. X. Kärtner, E. P. Ippen, and S. T. Cundiff, Femtosecond laser development, in Femtosecond Optical Frequency Comb: Principle, Operation and Applications, J. Ye and S.T. Cundiff, eds., Springer Verlag, 2005.
4. T. Udem, R. Holzwarth, T. W. Hänsch, "Optical frequency metrology," Nature 416, 233–237, 2002.
5. X. Liu, D. Du and G. Mourou, "Laser ablation and micromachining with ultrashort laser pulses," in IEEE Journal of Quantum Electronics, vol. 33, no. 10, pp. 1706-1716, 1997.
6. Denk, W., Strickler, J. H. & Webb, W. W. "Two-photon laser scanning fluorescence microscopy," Science 248, 73–76, 1990.
7. M. Nakazawa, T. Yamamoto, and K.R. Tamura, "1.28 Tbit/s-70 km OTDM transmission using third- and fourth-order simultaneous dispersion compensation with a phase modulator," Electron. Lett., 36, 2027-2029, 2000.
8. K. Carlsson, P. E. Danielsson, R. Lenz, A. Liljeborg, L. Majlöf, and N. Åslund, "Three-dimensional microscopy using a confocal laser scanning microscope," Opt. Lett. 10, 53-55, 1985.
9. Wu, Chiming and Niloy K. Dutta. “High-repetition-rate optical pulse generation using a rational harmonic mode-locked fiber laser.” IEEE Journal of Quantum Electronics 36 (2000): 145-150.
10. Seong-sik Min, Yucheng Zhao, Simon Fleming, "Repetition rate multiplication in figure-eight fibre laser with 3dB couplers," Opt. Commun. 277 (2), 411-413, 2007.
11. Gattass, R. R. & Mazur, E. "Femtosecond laser micromachining in transparent materials," Nat. Photonics 2, 219–225, 2008.
12. H. G. Weber et al., "Single channel 1.28 Tbit/s and 2.56 Tbit/s DQPSK transmission," 31st European Conference on Optical Communication,ECOC 2005, Glasgow, 2005, pp. 3-4 vol.6, 2005.
13. A. Bartels, T. Dekorsy, and H. Kurz, "Femtosecond Ti:sapphire ring laser with a 2-GHz repetition rate and its application in time-resolved spectroscopy," Opt. Lett. 24, 996-998, 1999.

14. Kerse, C., Kalaycıoğlu, H., Elahi, P. et al. "Ablation-cooled material removal with ultrafast bursts of pulses," Nature 537, 84–88, 2016.

15. Trillo et al. "Nonlinear dynamics of dual-frequency-pumped multiwave mixing in optical fibers," Physical review. A, Atomic, molecular, and optical physics 50 2, 1732-1747, 1994.

16. J. Fatome, S. Pitois and G. Millot, "20-GHz-to-1-THz Repetition Rate Pulse Sources Based on Multiple Four-Wave Mixing in Optical Fibers," in IEEE Journal of Quantum Electronics, vol. 42, no. 10, pp. 1038-1046, 2006.

17. A. Ryabtsev, B. Nie, and M. Dantus, "45 fs optical pulses from phase correctedbroadband cascaded four wave mixing products," Laser Phys. Lett. 10(12), 125109, 2013.

18. Z. Luo et al., "0.1–1-THz high-repetition-rate femtosecond pulse generation from quasi-CW dual-pumped all-fiber phase-locked Kerr Combs," IEEE Photon. J., vol. 8, no. 2, 2016.

19. J. Fatome et al., "Multiple four-wave mixing in optical fibers: 1.5–3.4-THz femtosecond pulse sources and real-time monitoring of a 20-GHz picosecond source," Opt. Commun., vol. 283, no. 11, pp. 2425–2429, Jun. 2010.

20. R. Slavik et al., "Stable and Efficient Generation of High Repetition Rate (>160 GHz) Subpicosecond Optical Pulses," in IEEE Photonics Technology Letters, vol. 23, no. 9, pp. 540-542, 2011.

21. A. C. S. Jr, J. M. C. Boggio, A. A. Rieznik, H. E. Hernandez-Figueroa, H. L. Fragnito, and J. C. Knight, "Highly efficient generation of broadband cascaded four-wave mixing products," Opt. Exp., vol. 16, no. 4, pp. 2816–2828, 2008.

22. Agrawal, G. P. Fiber-Optic Communication Systems, Wiley, 2010.

23. Quimby, R. S. Photonics and Lasers: An Introduction; John Wiley & Sons, Inc., 2006.

24. Agrawal, G. P. Nonlinear Fiber Optics, Academic Press, 2019.

25. Jacobsen RS, Andersen KN, Borel PI, Fage-Pedersen J, Frandsen LH, Hansen O, Kristensen M, Lavrinenko AV, Moulin G, Ou H, Peucheret C, Zsigri B, Bjarklev A. "Strained silicon as a new electro-optic material," Nature. May 11, 2006.

26. Timurdogan, E., Poulton, C., Byrd, M. et al. "Electric field-induced second-order nonlinear optical effects in silicon waveguides," Nature Photon 11, 200–206, 2017.

27. Z. Wu, S. Yang, H. Chen, M. Chen, and S. Xie, "Ultra high-repetition rate pulse sources based on cascaded four wave mixing in EYDF," IEEE Photon. Technol. Lett., vol. 29, no. 4, pp. 409–411, Feb. 15, 2017.

28. T. Inoue and S. Namiki, "Pulse compression techniques using highly nonlinear fibers," Laser Photonics Rev. 2(1-2), 83–99, 2008.

29. Dudley, J. M., Genty, G. & Coen, S. "Supercontinuum generation in photonic crystal fiber," Rev. Mod. Phys. 78, 1135–1184, 2006.

30. S. V. Chernikov, E. M. Dianov, D. J. Richardson, and D. N. Payne, "Soliton pulse compression in dispersion decreasing fiber," Opt. Lett. 18(7), 476–478 1993.

31. K. R. Tamura and M. Nakazawa, "54-fs, 10-GHz soliton generation from a polarization-maintaining dispersion-flattened dispersion-decreasing fiber pulse compressor," Opt. Lett. 26, 762-764, 2001.

32. Boyraz, O. & Jalali, B. "Demonstration of a silicon Raman laser," Opt. Express 12, 5269–5273, 2004.

33. Hanlon EB, Manoharan R, Koo TW, Shafer KE, Motz JT, Fitzmaurice M, Kramer JR, Itzkan I, Dasari RR, Feld MS. "Prospects for in vivo Raman spectroscopy," Phys Med Biol. Feb. 2000.

34. Lars Grüner-Nielsen, Marie Wandel, Poul Kristensen, Carsten Jorgensen, Lene Vilbrad Jorgensen, Bent Edvold, Bera Pálsdóttir, and Dan Jakobsen, "Dispersion-Compensating Fibers," J. Lightwave Technol. 23, 3566, 2005.

35. O. Lumholt, T. Rasmussen, and A. Bjarklev, "Modelling of extremely high concentration erbium-doped silica waveguides," Electron. Lett. 29(5), 495–496 (1993).

36. Ihor Pavlov, Emrah Ilbey, Ebru Dülgergil, Alper Bayri, and F. Ömer Ilday, "High-power high-repetition-rate single-mode Er-Yb-doped fiber laser system," Opt. Express 20, 9471-9475, 2012.

37. Jauregui, C., Limpert, J. & Tünnermann, A."High-power fibre lasers," Nature Photon 7, 861–867, 2013.

38. E. Desurvire, "Analysis of gain difference between forward- and backward-pumped erbium-doped fiber amplifiers in the saturation regime," in IEEE Photonics Technology Letters, vol. 4, no. 7, pp. 711-714, July, 1992.

39. Yılmaz, Saim & Elahi, Parviz & Kalaycioglu, Hamit & Ilday, Fatih. (2015). "Amplified spontaneous emission in high-power burst-mode fiber lasers," Journal of the Optical Society of America B. 32.

40. S. Pitois, J. Fatome, and G. Millot, "Generation of a 160-GHz transform-limited pedestal-free pulse train through multiwave mixing compression of a dual-frequency beat signal," Opt. Lett. 27, 1729-1731, 2002.

41. M. E. Fermann, M. J. Andrejco, Y. Silberberg, and M. L. Stock, "Passive mode locking by using nonlinear polarization evolution in a polarization-maintaining erbium-doped fiber," Opt. Lett. 18, 894-896, 1993.

42. Hasselbeck, M.P., NONLINEAR OPTICS, BASICS | Nomenclature and Units, in Encyclopedia of Modern Optics, R.D. Guenther, Editor. Elsevier: Oxford. p. 240-246, 2005.

43. Wang, Andong & Das, Amlan & Grojo, David. "Ultrafast Laser Writing Deep inside Silicon with THz-Repetition- Rate Trains of Pulses," Research (Wash D C), 2020.

44. Kalaycioglu, Hamit & Elahi, Parviz & Akcaalan, Onder & Ilday, Fatih. "High-repetition-rate ultrafast fiber lasers for material processing," IEEE Journal of Selected Topics in Quantum Electronics, 2018.

45. M. Chambonneau, Q. Li, M. Chanal, N. Sanner, and D. Grojo, "Writing waveguides inside monolithic crystalline silicon with nanosecond laser pulses," Opt. Lett. 41, 4875-4878, 2016.

46. Tokel, O., Turnalı, A., Makey, G. et al. "In-chip microstructures and photonic devices fabricated by nonlinear laser lithography deep inside silicon." Nature Photon 11, 639–645, 2017.

47. G. Matthäus, H. Kämmer, K. A. Lammers, C. Vetter, W. Watanabe, and S. Nolte, "Inscription of silicon waveguides using picosecond pulses," Opt. Express 26, 24089-24097, 2018.

48. I. Pavlov, O. Tokel, S. Pavlova, V. Kadan, G. Makey, A. Turnali, Ö. Yavuz, and F. Ö. Ilday, "Femtosecond laser written waveguides deep inside silicon," Opt. Lett. 42, 3028-3031, 2017.

49. M. Chambonneau, D. Richter, S. Nolte, and D. Grojo, "Inscribing diffraction gratings in bulk silicon with nanosecond laser pulses," Opt. Lett. 43, 6069-6072, 2018.

50. M. Chambonneau, D. Grojo, O. Tokel, F. Ö. Ilday, S. Tzortzakis, and S. Nolte, "In-Volume Laser Direct Writing of Silicon—Challenges and Opportunities," Laser & Photonics Reviews 15, 2021.